UC Irvine
UC Irvine Electronic Theses and Dissertations

Title
Global Continental Discharge and its Effects on Ocean and Climate

Permalink
https://escholarship.org/uc/item/2kw9s1nv

Author
Chandanpurkar, Hrishikesh Arvind

Publication Date
2016

Peer reviewed|Thesis/dissertation

eScholarship.org Powered by the California Digital Library
University of California

UNIVERSITY OF CALIFORNIA,
IRVINE

Global Continental Discharge and its Effects on Ocean and Climate

DISSERTATION

submitted in partial satisfaction of the requirements
for the degree of

DOCTOR OF PHILOSOPHY

in Earth System Science

by

Hrishikesh Arvind Chandanpurkar

Dissertation Committee:
Professor James S. Famiglietti, Chair
Professor Francois Primeau
Professor Keith Moore

2016

© 2016 Hrishikesh Arvind Chandanpurkar

Dedication

To infinite improbability, for making me privileged enough to get continuous opportunities to see this day;

To my heroes: George Orwell, Khalil Gibran, Phillip Pullman, Leonard Cohen, David Attenborough, Charlie Chaplin, and Sachin Tendulkar;

To the giants before me, for their curiosity about the nature of things, for their pursuit of truth while withstanding mass delusion;

To the United States of America, for jazz and the national parks;

To the UCI ESS department, for being a sanctuary to birds of a feather;

To my friends, with whom I can be, me;

To my uncle, and my school principal Mrs. Honwad, for introducing me to the beauty of nature;

To Aai and Aba, whose unconditional love and trust I had to once betray; and

To Juhi

Table of Contents

	Page
List of Figures	**v**
List of Tables	**vi**
Acknowledgements	**vii**
Curriculum Vitae	**viii**
Abstract of the Dissertation	**xi**
Chapter 1: Introduction	**1**
Chapter 2: How well observed is global continental discharge	**5**
2.1. Introduction and Background	6
2.2. Data and Methods	10
2.3. Results and Discussion	13
2.4. Conclusion	18
2.5. Acknowledgements	19
Chapter 3: Ocean's response to changes and uncertainties in continental discharge	**26**
3.1. Introduction and Background	27
3.2. Ocean's response to interannual changes in discharge	30
3.2.1. Experiment design	30
3.2.2. Results and Discussion	31
3.3. Ocean's response to realistic uncertainty in discharge forcing	31
3.3.1. Experiment design	32
3.3.2. Methods for discharge forcing data computation	33
3.3.3. Results and Discussion	34

3.4. Ocean's response to ice discharge from Antarctica 37

3.5. Conclusion 38

Chapter 4: Continental discharge from Aquarius Sea Surface Salinity 49

4.1. Introduction and Background 50

4.2. Data and Methods 52

4.3. Results and Discussion 54

4.3.1. Removal of *E-P* signal from SSS 54

4.3.2. Seasonal dynamics of major river plumes 56

4.3.3. Discharge estimation from the residual SSS anomalies 57

4.4. Conclusion 59

4.5. Acknowledgements 60

Chapter 5: Conclusion 66

5.1. Summary of Results 66

5.2. Implications for future work 67

References 70

Appendix 76

List of Figures

		Page
Figure 2.1	Time series of global ocean mass change estimates	21
Figure 2.2	Time series of global ocean atmospheric flux estimates	22
Figure 2.3	Time series of global continental discharge estimates	23
Figure 2.4	Comparison of global discharge estimates with ENSO3.4 Index	24
Figure 3.1	Fraction of σ in SSS	40
Figure 3.2	Locations of discharge forcing changes	41
Figure 3.3	Differences in SSS climatologies	42
Figure 3.4	Differences in stratification climatologies	43
Figure 3.5	Differences in near surface temperature climatologies	44
Figure 3.6	Differences in near MLD climatologies	45
Figure 3.7	Differences in near NPP climatologies	46
Figure 3.8	Relative uncertainty among the sensitivity cases	47
Figure 3.9	Ice discharge from Antarctica: changes in SST and sea ice area	48
Figure 4.1	Global distribution of SSS and *E-P*	61
Figure 4.2	Joint EOF analysis of SSS and *E-P*	62
Figure 4.3	Residual SSS anomalies in Atlantic Ocean	63
Figure 4.4	Residual SSS anomalies in Indian and Pacific Ocean	64
Figure 4.5	High variability regions of SSS anomalies, and discharge estimation	65
Figure A1	Time series of monthly anomalies in sea surface, steric height, and mass	76
Figure A2	Time series of global ocean precipitation and evaporation	77

List of Tables

		Page
Table 2.1	Summary statistics of *dM/dt*, *E-P*, and global discharge estimates	20
Table 2.2	Comparison of continent-wide estimates of discharge	25

Acknowledgements

First and foremost, I take this opportunity to express my gratitude toward my advisor, Prof. Jay Famiglietti, for giving me the opportunity to be a part of the program, providing uninterrupted funding, and giving me the freedom to choose a topic of my own liking and to pursue my ideas. I thank him for his invaluable input and guidance, as well as for his patience, all throughout the course of the last five years. I would also like to thank him for providing funding for several conferences and workshops, and for providing a very conducive office environment which added to my productivity.

I thank my committee members, Prof. Francois Primeau and Prof. Keith Moore, for their continuous guidance in this endeavor. J. T. Reager not only collaborated in this research, but also provided mentoring as well as scientific and technical guidance all throughout. I take this opportunity to express my thanks to Dr. Steve Yeager for hosting me at NCAR, and guiding me through the nitty-gritty of ocean modeling. I also acknowledge my co-authors Frank O. Bryan, Séverine Fournier, and Tajdarul Hassan Syed for their inputs.

I thank the NCAR Advanced Study Program for providing funding to visit NCAR.

I thank my colleagues in the ESS department and especially in the Famiglietti Group for their support.

This project wouldn't have been possible without continuous encouragement and love from my parents and from my wife.

Curriculum Vitae

Hrishikesh Arvind Chandanpurkar
Email: hchandan@uci.edu, (949) 698-2771

Education

2016	Ph.D. Candidate, Earth System Science University of California, Irvine, Irvine, CA
2009	M.Sc. Environmental Sciences University of Pune, Pune, India
2007	B.Sc. Geology Fergusson College, University of Pune, Pune, India

Additional Education

2010 – 2011	Post-Graduate Diploma in Geoinformatics Center for Development of Advanced Computing (CDAC), Pune, India
2008 – 2009	Post-Graduate Diploma in Sustainable Management of Natural Resources and Conservation Ecological Society, Pune, India
2005 – 2006	Diploma in Geopolitics and International Relations Jagannath Rathi Vocational Guidance and Training Institute, Pune, India

Research Experience

8/2015 – 1/2016	Graduate Visitor, Advanced Study Program (ASP), National Center for Atmospheric Research (NCAR), Boulder, CO
2011 – 2016	Research Assistant, University of California, Irvine, Irvine, CA
2009 – 2010	Assistant Environmental Analyst, VK:e environmental, Pune, India
2006 – 2009	Research Intern, Advanced Center for Water Resource Development and Management (ACWADAM), Pune, India

Publications and Selected Presentations

Chandanpurkar, H. A, S.G. Yeager, J.T. Reager, and J.S. Famiglietti (*in preparation*), Ocean's sensitivity to uncertainties in continental discharge, *Manuscript*

Chandanpurkar, H. A, F.O. Bryan, J.T. Reager, S. Fournier, and J.S. Famiglietti (*in preparation*), Continental discharge from Aquarius sea surface salinity observations, *Manuscript*

Chandanpurkar, H. A, J.T. Reager, J.S. Famiglietti, and T. H. Syed (*in preparation*), Revisiting mass-balance estimates of global continental discharge, *Manuscript*

Chandanpurkar, H. A, S.G. Yeager, J.T. Reager, and J.S. Famiglietti (2016), Role of continental discharge in ocean and climate dynamics through influence on ocean salinity, *Ocean Science Meeting, Oral presentation*

Chandanpurkar, H. A, S.G. Yeager, J.T. Reager, and J.S. Famiglietti (2016), Ocean's sensitivity to uncertainties in continental discharge, *CESM Ocean Model Working Group Meeting, Oral presentation*

Chandanpurkar, H. A, S.G. Yeager, J.T. Reager, and J.S. Famiglietti (2015), Sensitivity of ocean processes to changes and uncertainties in global river discharge, *American Geophysical Union Fall Meeting, Poster*

Chandanpurkar, H. A, J.T. Reager, T. H. Syed, and J.S. Famiglietti (2014), How much continental freshwater do global oceans receive? *Ocean Science Meeting, Poster*
Chandanpurkar, H. A, J.T. Reager, C. H. David, J.S. Famiglietti, and T. H. Syed (2012), Global runoff estimates derived from GRACE dataset*, American Geophysical Union Fall Meeting, Poster*
Chandanpurkar, H. A, and K.A. Subramanian (2008), Odonata of Naukuchiatal, a tectonic lake in Western Himalaya, India, *International Symposium of Odonatology, Poster*

Non-refereed publications
Chandanpurkar, H. A, and P. K. Moudgal (2011), Simulation of Glacial Lake Outburst Flood event for Northern Sikkim District, India*, Project Report, Center for Development of Advanced Computing*
Chandanpurkar, H. A (2009), Understanding the water resources in Naukuchiatal area of Nainital district, Uttarakhand, with special reference to the hydrogeological characters*, M.Sc. thesis, University of Pune*
Chandanpurkar *et al.*, (2007), Field based project of basic hydrogeology of Deccan basalt, *Project Report, Advanced Center for Water Resources Development and Management, Pune*

Awards and Grants

2016	Travel Grant for Summer School in Modeling Arctic Climate System, International Arctic Research Center (IARC), University of Alaska Fairbanks, USA
8/2015 – 1/2016	Advanced Study Program Grant for Graduate Visitor, National Center for Atmospheric Research (NCAR), Boulder, CO
2014	Travel Grant for CESM tutorial, National Center for Atmospheric Research (NCAR), Boulder, CO
2008	World Wildlife Fund grant to lead efforts to document Siberian Crane (*Leucogeranus leucogeranus*) species in northern India
2007	Dr. Anil Lalwani Award in Hydrogeology, Fergusson College, University of Pune, Pune, India

Professional Activities

2016	Journal Reviewer: *Climatic Change*
2012 – 2016	Member, American Geophysical Union

Computer skills
Python, Matlab, R, NCL, CDO, NCO, Shell scripting, UNIX, Fortran, IDL, ENVI, ERDAS Imagine, Leica Photogrammetry Suite, PCI Geomatica, ArcGIS, QGIS, GRASS GIS, Google Earth Engine, AutoCAD, Surfer, C, C++, Java, SQL, Git, LaTeX

Models
Model usage: CESM, CaMa-Flood, MODFLOW, HEC-RAS, ANUGA Hydro
Model Development: Co-developed a fully coupled carbon cycle box model for a graduate-level course project

Field Methods
Field hydrology and hydrogeology: Measuring water quality and quantity parameters, lake bathymetry, soil moisture, conducting pumping tests, geological mapping
Terrestrial ecosystems and biogeochemistry: Sampling biodiversity using quadrat, transect methods, measuring leaf gas exchange, soil CO_2 fluxes using LI-COR instruments

Teaching Experience

6/2015 – 7/2015	Lead Instructor, University of California, Irvine, Irvine, CA Undergraduate Course: Oceanography (63 Students)
2012 – 2016	Teaching Assistant, University of California, Irvine, Irvine, CA Introductory Undergraduate Courses: Oceanography (2012, 2015), The Atmosphere (2013) Advanced Undergraduate Courses: Data Analysis (2012, 2013), Remote Sensing (2016)
2014	Teaching Volunteer, Orange County Water Festival, Irvine, CA Live demonstrations about 'Environmental issues in the global oceans' to K-12 students
2012, 2013	Teaching Volunteer, Aquarium of the Pacific, Long Beach, CA Address queries at 'Ask a scientist' booth during 'NASA night' event
2012 – 2016	Guest Lecturer, University of California, Irvine, Irvine, CA Undergraduate Courses: Data Analysis (2012, 2013), Oceanography (2012), Remote Sensing (2016)
2013	Teaching Volunteer, Summer Camp, La Jolla Indian Reservation, CA Demonstrations about field hydrology methods
2008, 2010	Teaching Volunteer, University of Pune, Pune, India Field study of geology and biodiversity of Western Ghats for visiting undergraduate students from Salisbury University, MD

Informal workshops and teaching (in groups of more than 4)
Conducted workshops on diverse topics such as data analysis using Python; photographing earth system processes; basics of landscape photography; personal finance and investing for graduate students. Gave lessons on introduction and basics of playing mandolin

Service

2011	Volunteer, *in-situ* soil moisture measurement, CA
2010	Participant, Pune Bird Census, Pune, India
2009	Team leader, Great Himalayan Bird Count, Dehradun, India
12/2004 – 1/2005	Volunteer, Tsunami Relief Camp for 500 victims, Kerala, India
2002 – 2004	Member, National Cadet Corps, India (Rank: Lance Corporal)

Website: http://hrishikeshac.wix.com/hchandan
Blog: http://hrishichandanpurkar.blogspot.com

Abstract of the Dissertation

Global continental discharge and its effects on ocean and climate

By

Hrishikesh Arvind Chandanpurkar

Doctor of Philosophy in Earth System Science

University of California, Irvine, 2016

Professor James Famiglietti, Chair

Global continental discharge is an important component of global water cycle, but it is difficult to measure by traditional methods alone. In this dissertation, we provide an overview of current methods of estimating global continental discharge, and provide mass-balance estimates of global discharge using remote sensing and reanalysis products. Evaluating against observation-based estimates, we find that discharge computed from land mass balance using reanalysis-based moisture convergences and GRACE can provide a viable alternative to declining *in situ* observations' records for major river basins. Then we conduct a series of sensitivity experiments on an ocean-ice model forced with varying discharge to understand ocean's response to changes and uncertainties in discharge. We find that sea surface salinity (SSS), mixed layer depth, potential temperature, net primary production, and stratification show notable changes in the coastal and river plume regions, and that for certain river plume regions, interannual variability accounts to up to half of the total variance. Lastly, we introduce another novel method of estimating discharge from space. We isolate discharge and transport signal in SSS after removing atmospheric freshwater flux signal from SSS using joint EOF analysis, and then use discharge-SSS correlation to infer discharge for the Orinoco-Amazon, and Congo-Niger river basins.

Chapter 1

Introduction

Of all the components of the water cycle, perhaps the most familiar to humans is the surface runoff. Most ancient civilizations were based on the banks of rivers. Over a long period of time, after learning to store water through the building of dams, and to access groundwater through the building of wells, our direct dependence on river water has reduced to some extent. But rivers can still be considered as an effective indicator of water-cycle 'health', as they implicitly include contributions from precipitation, evapotranspiration, and water storage change. What makes surface runoff so familiar to us is that not only is it visible (unlike groundwater), but it is also easy to measure. It is possible to account for all the runoff upstream in the watershed by simply measuring the streamflow at a downstream location. Such a measurement would include surface runoff, as well as groundwater contribution to the runoff in the form of baseflow. Thus, it is more appropriate to collectively address surface runoff and baseflow[1] as basin discharge.

However, for a resource that is 'visible' and easy to measure locally, it is somewhat surprising, and admittedly disappointing, that we are not sure how much total surface runoff there is, globally, or how it is changing through time. The problem lies in the density of observations, management of gaging stations, and sharing of data. There are probably millions of streams and rivers on the planet, and observing each one of them is next to impossible. However, from these, only a few streams end up connecting with the ocean (exorheic), and monitoring their discharge would be sufficient in constraining our estimate of global surface runoff. But near

[1] Exception: A fraction of the baseflow might be sourced from the trans-watershed groundwater movement and the subsequent discharge measured may not truly reflect the basin discharge.

the coast, rivers typically form deltas and several tributaries, which makes measuring coastal discharge very difficult. And several coastal regions, such as mouths of rivers Amazon and Brahmaputra, are too inaccessible for regular monitoring. Also, the watershed boundaries don't necessarily correspond with political boundaries, and an upstream political entity seldom bothers to measure downstream discharge outside of its boundary.

Then there are issues concerning management of the gaging stations. The stations need to be maintained regularly as sediment built-up results in erroneous measurements. Also, as most of the gaging stations are government-owned, political stability is important for a long period of uninterrupted measurements. For example, when Soviet Union disintegrated, several gaging stations were left abandoned. Also, as water has become an important geopolitical resource, several countries are becoming more secretive about their water resource availability and usage. Currently, the Global Runoff Data Center (GRDC) hosted by the Federal Institute of Hydrology, Koblenz, Germany, and working under the auspices of the World Meteorological Organization (WMO) provides the most comprehensive observation data on global rivers. However, data from several major rivers, such as Ganga, Brahmaputra, Changjiang, and Yellow are not available; not because they are not measured, but due to restricted sharing policies of countries such as India and China. Due to all the above reasons, the total number of gaging stations that are active and share data has reduced dramatically since the 1970s [*GRDC*, 2015]. In fact, even within the 5-year span of this dissertation work, the number of active stations has reduced from about 3000 to about 1000.

Given this, a question one might ask is why one should care to accurately estimate the total continental discharge. This is a valid question. As mentioned above, global discharge is difficult to measure accurately and has almost no use for local or sometimes regional water

planning, policy, and management. Indeed, there have been very few research groups across the world that focus on global hydrology. However, in the wake of anthropogenic climate change, more and more researchers are looking at seemingly isolated processes from an 'earth system' perspective. We are realizing the intricate connections between natural processes and associated feedback loops. Understanding the 'whole' is becoming more important than understanding the 'sum of its parts'. A key term that is critical to our understanding of the current and future dynamics of Earth's climate is the global energy budget. Water being intimately related with energy, understanding and closing the global steady state water budget is also crucial. Also, due to the cyclical nature of water transport, changes in the discharge entering into the ocean could potentially, by affecting ocean fields and triggering changes in ocean-atmosphere and then atmosphere-land moisture flux and influencing land precipitation, result in changes in discharge, thus complete a runoff feedback loop.

This study explores our understanding of global continental discharge and its effects on ocean and climate. In recent years, due to advances in remote sensing technologies, multiple ways of estimating discharges have been developed. Information regarding water height changes can be obtained using satellite altimeters and radar interferometry. However, this approach requires additional information about the river width, and channel bathymetry, and can be applied to only large rivers. Alternatively, with the launch of the Gravity Recovery and Climate Experiment (GRACE) satellites, estimating changes in terrestrial water storage is possible for the first time at regional and global scales. This enables solving the water mass budgets for discharge, when combined with evaporation and precipitation data. In Chapter 2, we provide an overview of currently available global discharge data, and evaluate how mass-balance estimates

of global discharge compare with the current *in situ*-model hybrid data used as ocean model discharge forcing.

Although global river discharge is a relatively small component of the global water cycle, compared to evaporation and precipitation, it is relatively easier to measure, and is, therefore, typically used for evaluating performances of land surface models (LSM) and coupled earth system models (ESM). In most cases, the *in situ* discharge climatologies that are used for validation are assumed as 'truth', even though they may be from a different time period than the model experiments. Discharge time series are often oversimplified as being stationary. This can potentially lead to incorrect model parameterization. This is particularly true in the case of ocean sciences community. Oceanographers typically study large water fluxes, measured in Sverdrup ($1\ Sv = 1 \times 10^6\ m^3/s$), while total global continental discharge amounts to just about 1.2 Sv dispersed across the global coastline. Several upper ocean salt budget studies ignore continental freshwater flux, often due to lack of data, or use discharge climatologies. Available discharge forcing data reflect the limitations in observations, and are likely to result in less accurate model output than the model physics would allow. How do the inaccuracies in discharge forcing affect the model output? Which ocean fields are affected and to what degree? Which regions show most sensitivity to inaccuracies in discharge? We address these questions in Chapter 3, by conducting ocean-sea ice modeling experiments.

Surface ocean observations from space and in situ measurements have been growing in recent years. In Chapter 4, we explore if discharge signatures in the river plume regions can be effectively used for inferring discharge. We provide a novel way of removing atmospheric moisture flux from sea surface salinity measurements, and estimate discharge changes for two major river systems.

Chapter 2

How well observed is global continental discharge?

Abstract. Total continental freshwater discharge into the oceans is a key feature of the global water cycle, but is currently impossible to observe using ground-based methods alone. To characterize the uncertainty across existing modeling and satellite approaches, we present an ensemble of historic monthly global continental discharge estimates that enforce water mass balance over land and ocean. We combine independent measurements of ocean/land mass change from altimetry and GRACE with multiple estimates of evaporation minus precipitation (*E-P*) from remote sensing and reanalysis, to compute a 25-member ensemble time series of global discharge. Results reveal agreement in mass budget across approaches, but a large spread in global *E-P* estimates, resulting in a spread in discharge estimates. We find that discharges with reanalysis-based *E-P* provide a closer comparison with current observation-based estimates (RMS=5,700 km^3/yr; R=0.79). Combing GRACE- and altimetry-based mass change estimates with reanalysis-based moisture convergences, we provide total annual mean discharge for 2/1992-7/2015 as 38,700 ± 4,800 km^3/yr.

2.1. Introduction and Background

Continental discharge (i.e. from all land masses including Greenland and Antarctica) is the primary mechanism of freshwater transport from global land to the global oceans, and is the largest freshwater input to the oceans after precipitation [*Oki and Kanae*, 2006; *Trenberth et al.*, 2007]. Yet, our ability to measure discharge globally and continuously is limited by traditional instrumentation and methodologies [*Syed et al.*, 2005a]. River discharge is typically measured using streamflow gaging stations [e.g. *Couet et al.*, 2009]. Gaged observations are regarded as very accurate at the scale of measurement and are used as benchmark for calibration and validation of modeled estimates.

However, while *in situ* observations of continental discharge are an essential component of a terrestrial hydrologic observation system, they have several limitations. Gaging stations measuring river discharge to the oceans have inconsistent records due to variations in management practices [*Syed et al.*, 2005a], have sparse density near river mouths [*Dai and Trenberth*, 2002; *Dai et al.*, 2009], and are often inadequate to correctly record basinwide flooding events in floodplains and other flows that bypass the location of observation [*Syed et al.*, 2005a]. Also, there has been a decrease in the number of active gaging stations in recent decades [*GRDC*, 2015]. Furthermore, lack of public sharing of hydrologic data by several countries limits its availability and makes its retrieval challenging.

Land surface models (LSMs) are sometimes used to simulate continental discharge for global water cycle studies [*Milly et al.*, 2005], and for gap-filling and extrapolation of inconsistent and sparse *in situ* observations, and in some basins are the only available estimates of discharge. However, discharge generated using LSMs generally deviates from observations because the primary purpose of these models is not streamflow simulation. Hence, they lack

realistic representation of several critical hydrological processes [*Famiglietti and Wood*, 1994] such as baseflow, permafrost thawing, snow melt discharge [*Zaitchik et al.*, 2010; *Lawrence et al.*, 2012], or even basic elements of water management such as groundwater pumping and reservoir storage. Also, atmospheric forcing inaccuracies affect simulated discharge.

To overcome this, gaged observations are sometimes blended with modeled discharge to obtain a spatio-temporally consistent dataset [*Dai and Trenberth*, 2002; *Fekete*, 2002; *Dai et al.*, 2009; *Clark et al.*, 2015]. The most comprehensive and long-term estimates of global discharge in the last few years are from *Dai et al.*, [2009], and include gaged observations from the 925 largest exorheic (ocean draining) rivers. Unobserved discharge that occurs between gaging stations and the river mouth is estimated by regression using a station-to-mouth ratio of simulated discharge output from Community Land Model (CLM3) [*Oleson et al.*, 2004]. Temporal gaps in observations are filled through regression with nearby gaging stations or with simulated discharge, and the latter is also used to directly estimate discharge from unmonitored basins. These data are widely considered the 'best available' estimates of discharge and used as discharge forcing for ocean models as a part of Coordinated Ocean-Ice Reference Experiments (COREv2) interannual forcing data [*Large and Yeager*, 2009]. COREv2 data provides a common surface forcing data for ocean-sea ice model, enabling intercomparison studies complimenting the Coupled Model Intercomparison Project (CMIP) [*Danabasoglu et al.*, 2014, 2016; *Griffies et al.*, 2014].

However, hybrid approaches such as *Dai et al.*, [2009] inevitably inherit some of the demerits of observations and of simulated discharge discussed above. *Clark et al.*, [2015] used a similar approach to *Dai et al.*, [2009], but achieved a global mean discharge about 25% higher than *Dai et al.*, [2009], primarily because they used a different land surface model (Variable

Infiltration Capacity- VIC model). *Rodell et al.*, [2015] recently presented a comprehensive study of global water fluxes, optimizing multiple datasets for water and energy budget closure, which yielded a discharge estimate greater than *Dai et al.*, [2009], but less than *Clark et al.*, [2015]. With assumed future decreases in the availability of gaging station data, hybrid methods would be forced to rely more on simulated discharge, and as a result be even more susceptible to these large model biases. Furthermore, as the hybrid methods rely on the carefully established relationship between simulated runoff and observations at each station, automating such analysis is not desirable and as a result, providing regular updates to such approaches is tedious. For example, due to lack of availability of updated alternatives, COREv2 forcing data [*Large and Yeager*, 2009] use the discharge climatology (as opposed to the actual time series) from *Dai et al.*, [2009] since 2006.

Total continental discharge into the oceans can be estimated by solving the ocean mass balance:

$$R = \frac{d(M_{OCN})}{dt} - P_{OCN} + E_{OCN} \quad (2.1)$$

where M, P and E are mass of water, precipitation, and evaporation, respectively, and the subscript OCN implies ocean. Similarly, discharge (R) estimates at basin as well as at continental scale can be obtained by solving the land mass balance:

$$R = P_{LND} - E_{LND} - \frac{d(M_{LND})}{dt} \quad (2.2)$$

where the subscript LND implies land, and M_{LND} refers to the total mass of freshwater. *Syed et al.*, [2010] demonstrated that equation 1 can be solved for discharge using remote sensing datasets alone. Ocean mass is an important term in equations (2.1) and (2.2), and can be estimated from sea surface height from satellite altimetry after correction for steric height

changes, and since 2002, can be observed directly with NASA's Gravity Recovery and Climate Experiment (GRACE) mission [*Chambers et al.*, 2004]. Remote sensing-based global precipitation data such as Global Precipitation Climatology Project- GPCP [*Adler et al.*, 2003] and Climate Prediction Center Merged Analysis of Precipitation- CMAP [*Xie and Arkin*, 1997], and ocean evaporation data such as Objectively Analyzed Ocean Atmosphere Fluxes- OAFlux [*Yu et al.*, 2008], and SeaFlux [*Curry et al.*, 2004] are available. This enables solving ocean mass balance (equation 2.1) entirely using remote sensing-based data. Remote sensing- and reanalysis-based discharge estimates have several advantages relative to ground-based measurements: They negate the density and management inconsistencies and are free from the data-sharing limitations of *in situ* observations; they include all subsurface flow (baseflow as well as submarine groundwater discharge [Syed et al., 2005]); they are temporally coherent; inter-mission biases can be removed during mission overlap period (e.g. as with satellite altimeters); and they can be updated in real or near-real time. They also include discharge from ice-sheets, which traditionally is difficult to measure.

The process of land evapotranspiration (*ET*) is often more complex than ocean evaporation due to heterogeneity in surface properties, and hence, is typically poorly observed and simulated [*Wang and Dickinson*, 2012]. Few remote sensing based *ET* data are available, and reanalysis-based estimates of *P* and *E* suffer spurious trends due to changes in observations [*Trenberth et al.*, 2011] and measurement biases, though newer reanalysis products perform somewhat better [*Trenberth and Fasullo*, 2013b; *Rodell et al.*, 2015]. However, the term *P*-*E*, i.e. net precipitation, can also be obtained applying the atmospheric moisture budget as:

$$\frac{dW}{dt} + \nabla.\mathrm{Q} = -(\mathrm{P} - \mathrm{E}) \qquad (2.3)$$

where W is total column-integrated water vapor and $\nabla.Q$ is the horizontal divergence of moisture flux. *Syed et al.,* [2005, 2009] demonstrated that convergence based *P-E* can be used for estimating basin-scale to continental-scale discharge. *Trenberth et al.*, [2011], *Trenberth and Fasullo*, [2013a, 2013b] provide comprehensive evidence that reanalysis *P-E* computed from the convergence term, are much more accurate than the reanalysis *P-E* estimates, especially in the newer generation of reanalysis data.

In this study, in addition to updating the analyses of *Syed et al.*, [2009] and *Syed et al.*, [2010], we take advantage of several datasets to provide a comprehensive comparison of ocean and land mass-balance discharge estimates from remote sensing and reanalysis. Novel aspects of this work include the first use of a multi-mission altimetry data with global coverage as well as mass change estimates from GRACE, and we use five state-of-the-art reanalysis data products to account for the variability in the reanalysis moisture convergence fields. More generally, we quantify and discuss the mean, trend, and uncertainty in our discharge estimates. We evaluate our estimates relative to the *Dai et al.*, [2009] observation-based data at seasonal and interannual time scales. We then compare our land-based estimates with *Dai et al.*, [2009], *Clark et al.*, [2015], and *Rodell et al.*, [2015] for continent-wide discharges. Finally, we discuss the potential of land-based mass balance as a viable method to provide discharge forcing to global ocean simulations.

2.2. Data and methods

We solve equations (2.1) and (2.2) for *R* using various combinations of *dM/dt* and *P-E*. We use the newly-released GRACE mass concentration (or 'mascon') solution from NASA JPL (JPL-RL05M) [*Watkins et al.*, 2015] to compute *dM/dt* over land and ocean. JPL-RL05M

solution links an analytically expressed mascon function with measurements of range-rate between the two GRACE satellites to directly estimate mass variations over 4451 equal-area mascons across Earth's surface. A key advantage of mascon solution over a traditional spherical harmonics solution is that JPL-RL05M uses a priori information from geophysical models and observations as a constraint, and hence neither suffers from North-South striping, nor loses data due to the counter destriping. The data are also corrected for signal leakage at the ocean-land boundary. In this study, by masking out the ocean (land), aggregating into a single time series, and taking the monthly derivative, we compute *dM/dt* over the land (ocean). To ensure consistency with ocean *dM/dt*, we include Greenland and Antarctica in our land mask.

We obtain ocean *dM/dt* from altimetry by removing the steric signal from sea surface height anomalies (SSHA) and taking monthly derivatives. SSHA are obtained from Archiving, Validation and Interpretation of Satellite Oceanographic data (AVISO), processed with Ssalto multimission ground segment (SSALTO)/ Data Unification and Altimeter Combination System (DUACS) system. The SSALTO/ DUACS system merges data from several satellite missions, including, ERS-1, ERS-2, Envisat, Jason-1, Jason-2, TOPEX/Posidon, Cryosat-2, Y-2A, and SARAL-Altika. Detailed processing steps for each dataset, as well as cross-calibration and merging is described in *AVISO*, [2015].

An important advantage of the SSALTO/DUACS data product is its global coverage. Not being limited to 66°N/S (as in [*Syed et al.*, 2010]) enables a much more robust comparison with GRACE, while it eliminates the uncertainty due to mass fluxes at data boundary latitudes. We use Version 4 of Met Hadley Center's EN series (EN4, [*Good et al.*, 2013]) of objectively analyzed subsurface temperature and salinity fields, that are corrected for instrument-bias following *Levitus et al.*, [2009], to compute the steric signal in the top 2000m of global ocean.

Input data for EN4 include the World Ocean Database 2009, as well as Argo floats [*Davis et al.*, 2001] in recent years. The Steric Height Anomaly (SHA) is obtained by integrating computed specific density across each depth level from temperature, salinity, and depth-derived pressure fields following *IOC et al.*, [2010] The time series of SSHA, SHA, as well as mass anomalies from GRACE are shown in Figure A1 in the Appendix.

The *E-P* fields over land and ocean are obtained from equation (2.3). Vertically integrated zonal and meridional moisture fluxes and precipitable water (total column water vapor) fields are used to compute total column horizontal moisture flux divergence and precipitable water tendency. The fields are obtained from five state-of-the-art reanalysis products, including the ECMWF interim reanalysis (ERA-I) [*Dee et al.*, 2011], the Japanese 55-year Reanalysis (JRA-55) [*Kobayashi et al.*, 2015], the NASA Global Modeling and Assimilation Office (GMAO) Moderate Era Retrospective-Analysis for Research and Applications - MERRA [*Rienecker et al.*, 2011] and MERRA-2 [*Bosilovich et al.*, 2015], and the National Centers for Environmental Prediction (NCEP) Climate Forecast System Reanalysis-CFSR [*Saha et al.*, 2010]. ERA-I and JRA-55 include 4D variational assimilation, a significant improvement from their predecessors, while MERRA and MERRA-2 involve an Incremental Analysis Update (IAU) procedure that adjusts modeled states based on observed states. CFSR includes several key updates to all components in the NCEP Climate Forecast System (CFS) model.

Over the ocean, in addition to reanalysis, we use two satellite-based products for ocean precipitation and evaporation. We use the GPCPv2.2 [*Adler et al.*, 2003] and CMAP [*Xie and Arkin*, 1997] merged precipitation data from multiple satellites and *in situ* observations. Ocean evaporation data are from the OAFlux [*Yu et al.*, 2008], and SeaFlux [*Curry et al.*, 2004]

datasets. OAFlux data are derived from merging satellite estimates, *in situ* measurements of observable variables from Voluntary Observing Ships (VOS), and reanalysis products. SeaFlux data are purely satellite-based, and are generally considered as the most accurate satellite-based observations of ocean evaporation. The time series of global ocean precipitation from GPCP and CMAP, and evaporation from OAFlux and SeaFlux are shown in Figure A2 in the Appendix. As *Dai et al.*, [2009] was used in the COREv2 analysis in closing energy and water budgets, for comparison we also include COREv2 *P* and *E* in our analysis. COREv2's *P* is a latitude-based combination of GPCP and CMAP, while *E* is based on NCEP reanalysis. Detailed information on generation of CORE fluxes can be found in *Large and Yeager*, [2009].

Once the *dM/dt* and *P-E* time series are computed, a low-pass filter of 5 months is applied to highlight semi-annual and lower frequencies. Discharge is then computed for each combination of *E, P, P-E*, and *dM/dt*. Thus, in all, 25 estimates of global discharge are obtained. From this, estimates are grouped based on their component source and type (ocean, land, remote sensing, reanalysis, and *dM/dt* method), and ensemble means are generated for each discharge group. Uncertainty in each category is estimated as the highest RMS error of an individual member with the ensemble mean. Thus, the uncertainty represents the spread of the ensemble members around the ensemble mean.

2.3. Results and Discussion

Figure 2.1 shows the *dM/dt* time series from GRACE over the ocean (blue) and land (yellow dotted line, inverted), as well as from altimetry (black). Also shown is *dM/dt* (red) obtained from solving equation 1 from COREv2 *P*, *E*, and *R* (from *Dai et al.*, [2009]). Shaded areas represent $\pm 1\sigma$ uncertainty for each monthly time series. As the global mass is conserved

while processing GRACE mascon data, mass anomalies over land, when inverted, are identical to those from over ocean. *dM/dt* time series computed from altimetry (after removing steric signal) matches very well with those from GRACE land and ocean, with R=0.9 and RMS error of 6,810 km^3/yr over the overlapping period. Where as *dM/dt* from COREv2 shows relatively poor comparison with both *dM/dt* from altimetry (R=0.62; RMS=13,700 km^3/yr) and from GRACE (R=0.77; RMS=8,630 km^3/yr) for the corresponding overlapping periods.

The next component of the mass balance, *E-P* is shown in Figure 2.2. The top plot shows various combinations of *E-P* estimates from remote sensing, while the bottom plot shows moisture convergence estimates from reanalysis over the ocean (moisture convergences over land, when inverted, are nearly identical to those over ocean, hence not shown separately). The remote sensing estimates of *E-P* show a wide spread, with RMS among the time series ranging from 14,000 to 27,400 km^3/yr, and R ranging from -0.06 to 0.78. This poor intercomparison is largely due to the differences in ocean evaporation data from SeaFux and OAFlux. Moisture convergences from reanalysis also show a spread across the mean (though relatively small; RMS ranging between 3,200 and 13,000 km^3/yr), but show remarkably good correlation (R ranging between 0.85 and 0.94).

The characteristics of *dM/dt* and *E-P* accrue in the water balance discharge estimates, as seen in Figure 2.3. The top plot shows all 20 of ocean mass-balance estimates of global discharge. Ensemble averages are color-coded, while individual time series in the ensembles are shown in lighter shades with same color-coding. In the plot labels, 'A', 'G', 'RS', and 'RE' represent altimetry-based *dM/dt*, GRACE based *dM/dt*, remote sensing-based *E-P*, and reanalysis-based *E-P*. For comparison, observation-model hybrid estimate from *Dai et al.*, [2009] (green), and discharge estimates computed with COREv2 *E-P* with GRACE (magenta)

and altimetry (red) *dM/dt* are also shown. The bottom-left plot shows the seasonal climatology of ensemble means, and the bottom-right plot shows the interannual time series after passing the monthly time series through a 13-month window of moving average. Table 2.1 includes summary statistics of several time series shown in Figure 2.1-2.3.

It is evident from Figure 2.3 and from Table 2.1, that all the mass-balance estimates of discharge show reasonable agreement for mean annual discharge, and match well with that from observation-based hybrid discharge from *Dai et al.*, [2009] (with the added time-invariant discharge of 2300 km^3/yr from Antarctica, as a part of COREv2 flux). Reanalysis-based discharges from land and ocean mass balance show remarkably closer mean, seasonal, and interannual variability to *Dai et al.*, [2009] estimates. However, the remote sensing-based discharges show distinctly higher seasonal amplitude and interannual variability compared to *Dai et al.*, [2009] and reanalysis-based estimates. Considering 10-20 % error in gaged values in *Dai et al.*, [2009], their reliance on model output to account for about 30% of total global discharge, and that subsurface discharge into the ocean is not included in the gaged observations but is implicitly included in the mass-balance estimates presented here, it is possible that the amplitude of seasonal and interannual variability are not fully represented in *Dai et al.*, [2009] data. Hence in order to understand whether it is practically possible to have the seasonal amplitudes as seen in remote sensing-based discharge estimates, we conducted an experiment wherein we optimized the *Dai et al.*, [2009] data to have maximum seasonal amplitude at each coastal grid point without resulting in negative discharge. The overall amplitude increase was modest and incapable of explaining the higher amplitude seen in remote sensing based estimates, even in this extreme (and less likely) scenario.

Trends associated with our discharge time series are provided in Table 2.1. As *dM/dt* estimates from both altimetry and GRACE do not show significant trends, the trends in discharge estimates come from *E-P* estimates. Discharges with remote sensing-based *E-P* show significant increasing trends (400±100 km^3/yr^2 for 1993-2015 from altimetry-based mass balance and 315 km^3/yr^2 for 2002-2015 from GRACE-based mass balance) that are comparable to increasing trends reported in remote-sensing based ocean mass-balance study by *Syed et al.*, [2010]. The minor differences in our trends and those found by *Syed et al.*, [2010] arise from not including some datasets such as HOAPS, comparing different time lengths, and using updated versions of all datasets. Discharges with reanalysis-based *E-P*, however, do show non-significant to significant downward trends. As all the time series show a general downward trend since 2009-2010, trend estimates from GRACE-based discharge are more influenced by these years owing to the shorter record of GRACE compared to altimetry.

Owing to overall agreement between the reanalysis-based discharge estimates with *Dai et al.,* [2009], we further explore their interannual variability with respect to ENSO events. Figure 2.4 compares our ocean mass-balance estimates of discharges with reanalysis-based *E-P*, altimetry (black), and GRACE (yellow) with Nino3.4 index (red, dotted) obtained from https://www.ncdc.noaa.gov/. Nino3.4 is a commonly used index to represent different ENSO phases. The index time series is already smoothed with 3-month running mean (in order to compute the index), so an additional 10-month running mean is computed to offer robust comparison with the 13-month smoothed discharge time series. Also, as there is inverse relationship between discharge and ENSO, the index time series is inverted in the figure. For comparison, *Dai et al.,* [2009] discharge time series (green) is also provided. All four time series are normalized to account for differences in the units. GRACE and reanalysis based estimates of

mass balance over land are identical to those from ocean mass balance (yellow), and hence are not included. The mass-balance discharges show better correlation with mass-balance discharge using altimetry (R=-0.6) compared to *Dai et al.,* [2009] data (R=-0.41), and mass-balance discharge using GRACE (R=-0.43), though the difference in the overlapping periods likely influences the intercomparison.

Owing to overall agreement between various reanalysis-based *E-P*, we combine by computing arithmetic mean, all land water and ocean mass balance estimates of discharge estimates based on *E-P* from reanalysis and *dM/dt* from altimetry and GRACE. The mean global continental discharge thus obtained, for 2/1992-7/2015 is 38,700 ± 4,800 km^3/yr. The uncertainty estimate on the long-term mean is standard deviation of the long-term mean estimates of 15 individual discharge time series that were combined. The combined mean discharge shows insignificant trend of -4 km^3/yr^2 with 95% confidence interval of ± 40 km^3/yr^2. The combined discharge compares well with observation-model-based hybrid discharge from *Dai et al.,* [2009], with RMS=5,700 km^3/yr (which equals to about 15% of the long-term mean), and R=0.79.

Mass-balance estimates with GRACE and reanalysis-based *E-P* over land also enables computing continent- and basin-scale estimates. Table 2 lists continent wide estimates of land-based discharge compared to those from *Dai et al.,* [2009], *Clark et al.*, [2015] and *Rodell et al.*, [2015]. Even though the time periods of these studies differ, and there might be added uncertainties associated with usage of different regional masks, the results are seasonably comparable. Mass-balance-based discharge from Australia-Oceania is higher compared to others, and much of the difference comes from Indonesia, while discharges from Africa and Eurasia are lower compered to others. Our *dM/dt* and discharge components for the two ice sheets are similar to *Rignot et al.*, [2011].

2.4. Conclusion

This work provides a summary of the current state of our ability to measure global river discharge into the oceans from various methods. It further explores the mass balance approaches over land and ocean, which provide a simple yet compelling method for estimating global continental discharge. We demonstrate that ocean mass change, a critical component of mass balance, is similar when measured by two independent remote sensing methods, thus providing us confidence in both the methods. The global discharge estimate by *Dai et al.*, [2009], despite limitations elaborated in the introduction, helps in filtering out the less accurate (remote sensing) estimates of *E-P* from the better ones (moisture convergences from reanalysis). Based on this, we provide the estimate of mean annual global continental discharge as $38{,}700 \pm 4{,}800$ km^3/yr.

The discharge computed from land water mass balance using reanalysis and GRACE not only agrees well with observation-based data, but also has the ability to provide discharge estimates based on variable domains (i.e. basins/continents/oceans), and is a good candidate for use in a spatially gridded product of global discharge into the oceans, as a potential alternative to *Dai et al.*, [2009] . Thus, mass-balance estimates of global river discharge provide an important complement to on-site gaging measurements and to other off-site approaches [*Mersel et al.*, 2013; *Gleason and Smith*, 2014], including the upcoming Surface Water and Ocean Topography (SWOT) satellite mission [*Alsdorf et al.*, 2007; *Durand et al.*, 2010]. The estimates presented here will only get better with more high-resolution datasets, next-generation of reanalysis, and will provide a viable discharge product in the pre-SWOT years and provide complementary discharge estimates to SWOT.

2.5. Acknowledgments

We gratefully acknowledge University of California Office of the President Multicampus Research Programs and Initiatives and the NASA IDS Sea Level program for supporting this research. The datasets used in this study were acquired from following sources. GRACE: http://grace.jpl.nasa.gov; Reanalysis data ERA-I: http://apps.ecmwf.int, JRA55: http://rda.ucar.edu, MERRA and MERRA-2: http://goldsmr2.sci.gsfc.nasa.gov, and CFSR: ftp.cgd.ucar.edu; Altimetry: http://www.aviso.altimetry.fr; Ocean temperature and salinity dataset: http://www.metoffice.gov.uk; GPCP and CMAP: http://www.esrl.noaa.gov; and OAFlux: ftp://ftp.whoi.edu. Authors would like to thank Dr. Steve Yeager of NCAR for providing the COREv2 *P*, *E*, and *R* data. A portion of this work was conducted at the Jet Propulsion Laboratory, California Institute of Technology, under contract with NASA.

Table 2.1. The mean, standard deviation, and the trend for several of the computed time series. 95% confidence intervals are provided for the mean and the trend. Trends are computed after removing the seasonal cycle. 'A', 'G', 'RS', and 'RE' represent altimetry-based *dM/dt*, GRACE-based *dM/dt*, remote sensing-based *E-P*, and reanalysis-based *E-P,* respectively.

Variable	**Data**	**Time period**	**Mean** ($km^3\ yr^{-1}$)	**σ** ($km^3\ yr^{-1}$)	**Trend** ($km^3\ yr^{-2}$)
dM/dt	G	5/2002-4/2015	620±2,100	13,400	50±50
dM/dt	A	2/1993-7/2015	860±1,900	16,100	9±30
dM/dt	COREv2 $_{(P-E+R)}$	2/1993-12/2006	2,500±2,000	13,300	-120±270
E-P	Ensemble RS	2/1993-7/2015	30,300±1,100	9,400	390±100
E-P	Ensemble RE	2/1993-7/2015	37,800±980	8,200	-10±40
R	A + $(E-P)_{RS}$	2/1993-7/2015	32,000±1,800	14,800	400±100
R	A + $(E-P)_{RE}$	2/1993-7/2015	38,700±1,100	9,300	-3±40
R	G+ $(E-P)_{RS}$	5/2002-4/2015	33,300±1,800	11,300	280±210
R	G+ $(E-P)_{RE}$	5/2002-4/2015	38,500±1,100	7,100	-175±70
R	A + $(E-P)_{COREv2}$	2/1993-12/2006	42,200±2,600	17,100	90±290
R	G + $(E-P)_{COREv2}$	5/2002-12/2006	39,400±3,600	13,400	-1,400±840
R	Dai *et. al* [2009]	2/1993-12/2006	39,800±1,200	8,100	-20±30

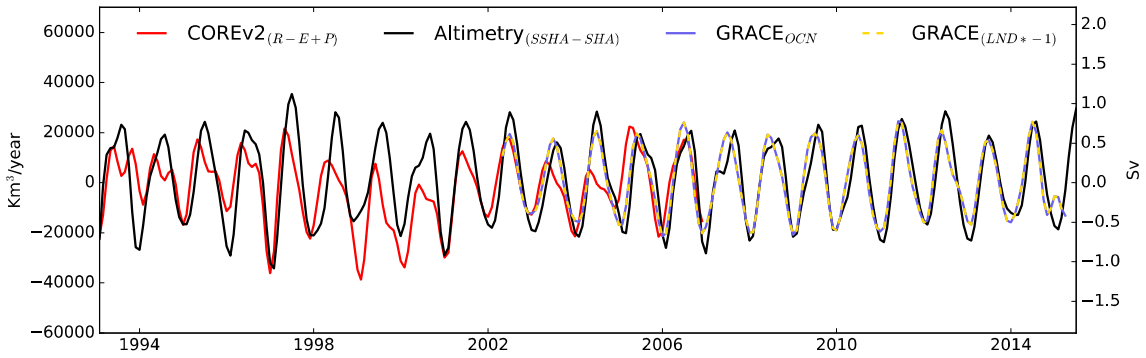


Figure 2.1. Global ocean mass change (*dM/dt*) estimates from altimetry (black; after removing the steric signal), GRACE over ocean (blue), GRACE over land, inverted (yellow, dotted), and COREv2 (red). Units are expressed in Km^3/yr (left-side Y axis), and in Sverdrup (right-side Y axis). Shaded areas represent $\pm 1\sigma$ uncertainty.

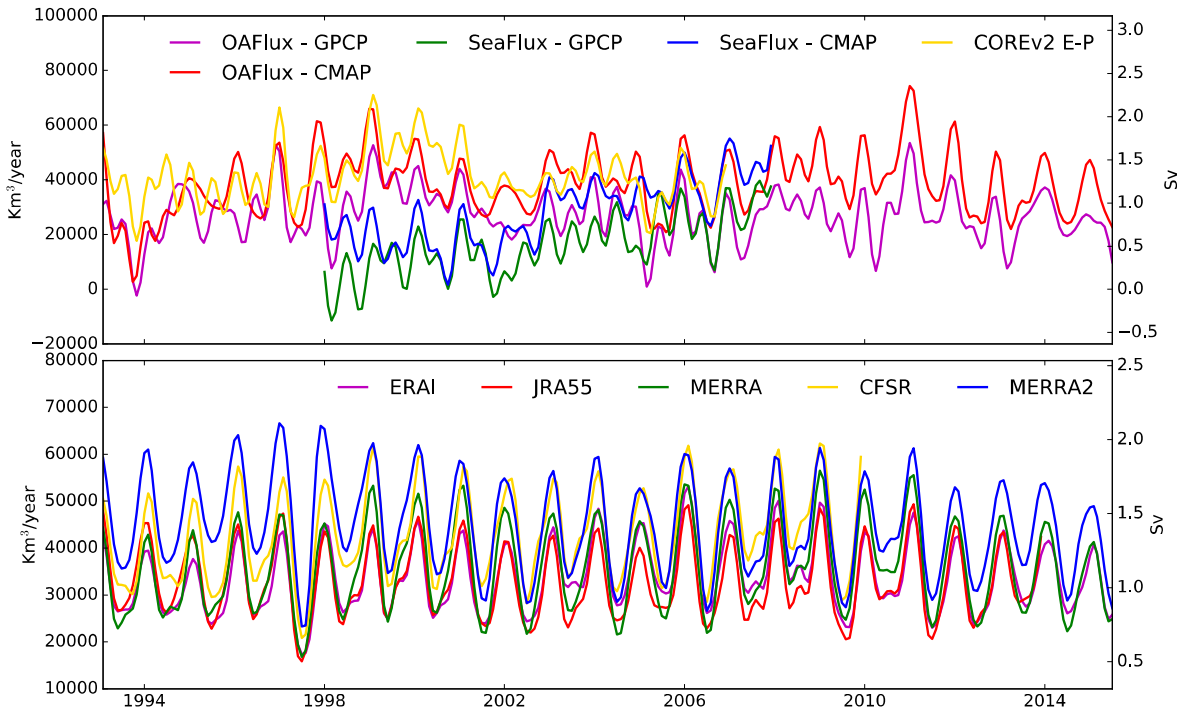


Figure 2.2. *E-P* estimates over global oceans. (Top) from combinations of various remote sensing *P* and *E* datasets, and (bottom) from moisture convergences from five reanalysis datasets over global ocean. Units are expressed in Km^3/yr (left-side Y axis), and in Sverdrup (right-side Y axis)

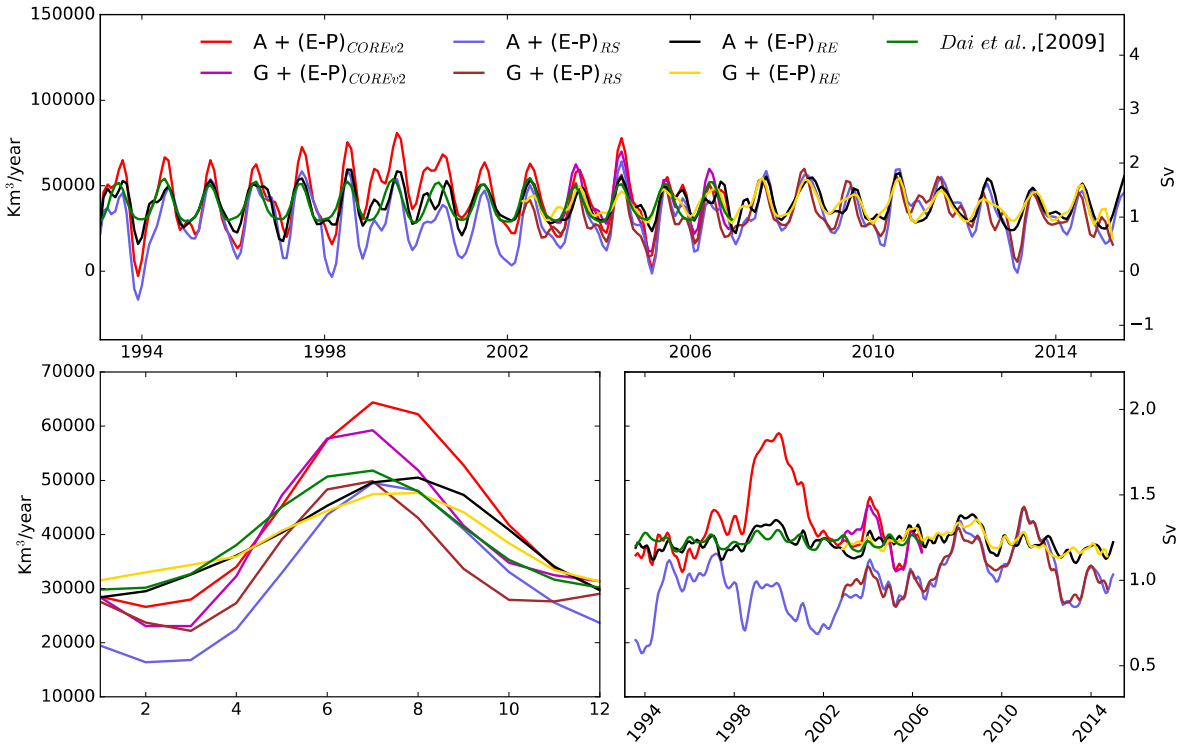


Figure 2.3. 20 time series of global continental discharge from ocean mass-balance, color-coded according to ensembles based on type of *E-P* ('RS': remote sensing, 'RE': reanalysis, and COREv2), type of *dM/dt* ('A': altimetry and 'G': GRACE). The Dai *et al.,* [2009] estimate from COREv2 is also shown (green). (bottom, left) Climatology of the ensemble means. (bottom, right) Discharge ensemble means after 13-month smoothing. Units are expressed in Km^3/yr (left-side Y axis), and in Sverdrup (right-side Y axis).

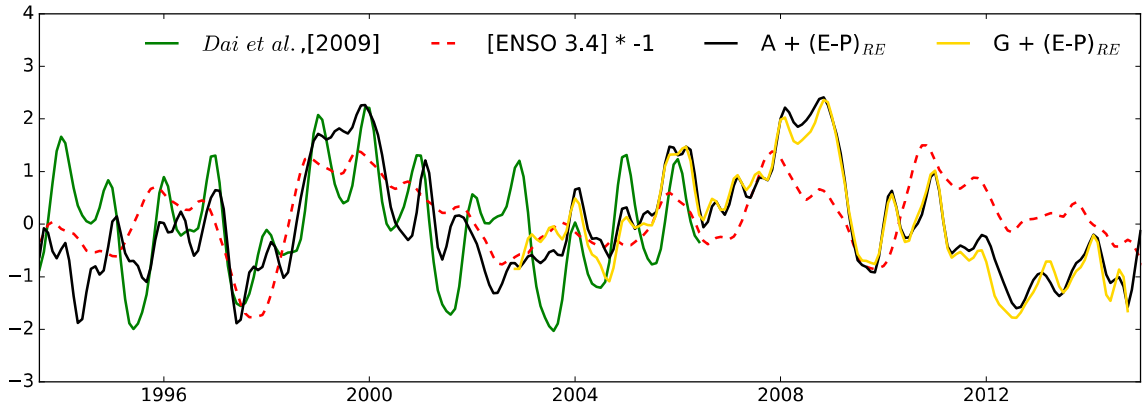


Figure 2.4. Normalized, 13-month smoothed time series of *Dai et al.,* [2009], mass-balance estimates of discharge from reanalysis-based *E-P* and *dM/dt* from altimetry (black), and GRACE (yellow) compared with 10-month smoothed Nino3.4 index, inverted (red, dotted)

Table 2.2. Mean annual discharge $km^3\ yr^{-1}$ based on continents and oceans. The uncertainties on our estimates are 95% confidence intervals over the mean. Uncertainty is not provided for Dai *et al.,* [2009].

	This work	**Dai *et al.*, [2009]**[2]	**Clark *et al.*, [2015]**[3]	**Rodell *et al.*, [2015]**[4]
	2002-2015	1949-2004	1950-2008	2000-2010
S. America	11,500±440	11,800	13,200±2,430	12,300±1,000
N. America	5,800±350	6,300	7,100±280	7,900±790
Africa	2,600±350	3,800	3,800±720	3,800±330
Eurasia	10,000±1,100	12,900	16,200±750	16,000±1,600
Australia-Oceania	5,600±390	1,200	3,400±120	3,600±410
Antarctica	2,400±100	2,300	-	2,300±240
Greenland	1,000±110	60	-	-
Global	38,900±2,800	38,400	44,200±2,700	45,900±4,400

[2] Values as mentioned in Clark *et al.,* [2015] except for Antarctica where values from COREv2 version of discharge are provided

[3] Excludes discharge from Greenland and Antarctica

[4] Greenland discharge is implicitly included in N. America estimate

Chapter 3

Ocean sensitivity to uncertainties in continental discharge forcing

Abstract. Freshwater flux into the ocean in the form of continental discharge influences several ocean properties and processes, such as surface salinity, temperature, mixed layer depth, and causes stratification, which influences several other fields. There are uncertainties in the present estimates of discharge, and how they affect our understanding of the ocean has not been studied. In this study, we run a series of global ocean-ice modeling experiments with varying discharge forcing and analyze the ocean's response to discharge changes and uncertainties. We find that interannual variability in discharge forcing is important and constitutes up to 50% of the variance in certain river plume regions. Differences in discharge forcing introduces a spread of up to 4 PSU in SSS, 2°C in near surface temperature, 50m in MLD, and about 0.4 PgC/year in NPP. The effects are limited to coastal and river plume regions. Changing discharge from Antarctica from liquid to ice discharge, results in decrease in surrounding SST by up to 1.3°C, and increases sea ice extent by up to 20%.

3.1 Introduction and background

The flux of freshwater from the land into the oceans is an important component of the global hydrologic cycle, and influences several ocean properties and processes. The addition of freshwater reduces the sea surface salinity (SSS) regionally, which leads to a decreased mixed layer depth (MLD). In a salinity-driven mixed layer, the pycnocline is governed by the halocline, and this can potentially create a barrier layer from the top of the halocline to the top of the thermocline [*de Boyer Montégut et al.*, 2007; *Kara et al.*, 2003; *Lukas and Lindstrom*, 1991; *Sprintall and Tomczak*, 1992].

The upper ocean stratification, governed by the freshwater fluxes, influences several ocean processes and properties. These include sea surface temperature (SST) [*Foltz and McPhaden*, 2009], ocean-atmosphere energy fluxes, oceanic heat and transport [*Godfrey and Lindstrom*, 1989], oceanic carbon uptake [*Sarmiento et al.*, 1998], marine primary productivity [*Polovina et al.*, 1995], upper ocean circulation and meridional overturning circulation (MOC) [*Rahmstorf*, 2002], and sea ice thickness and extent [*Aagaard and Carmack*, 1989]. Furthermore, a large barrier layer thickness (BLT) enhances heat build-up which is associated with El Nino Southern Oscillations (ENSO) [*Lukas and Lindstrom*, 1991; *Maes et al.*, 2002] and is also attributed to increased hurricane intensity [*Balaguru et al.*, 2012].

Several researchers have studied the sensitivity of various ocean properties to freshwater fluxes [*Aagaard and Carmack*, 1989; *Durand et al.*, 2011; *Hu et al.*, 2011; *Rahmstorf*, 1995; 2002; *Rennermalm et al.*, 2007; *Stouffer et al.*, 2006; *Weaver et al.*, 1991]. However, these studies focus on specific ocean processes and are mostly conducted at a regional scale. None of these works studied the effect of continental runoff on ocean processes at a global scale. Also, the sensitivity experiments typically involve large amounts of freshwater injected, or 'hosed'

within a relatively small area. Such freshwater forcing in the hosing experiments is often unrealistic.

In section 3.1., we discussed merits and demerits of several methods of estimating global continental discharge, such as *in situ* gauge station observations, land surface model runoff outputs, observations-model hybrid estimates, and provided mass-balance estimates using remote sensing and reanalysis. Specifically, we compared our mass-balance estimates with observation-model hybrid data from *Dai et al., [2009]* which is widely used for forcing ocean models as a part of COREv2 surface freshwater fluxes. We made a case for mass-balance estimates of discharge using GRACE-based *dM/dt*, and moisture convergences from reanalysis (as a proxy for *E-P*), as a potential alternative to *Dai et al., [2009]* data for ocean forcing, owing to the latter's inherent demerits, including its unavailability since 2006. We also saw the relative biases in reanalysis-based *E-P* estimates. How do the current limitations and challenges in measuring discharge, and the resultant uncertainty associated with the estimates affect ocean and climate?

One way to understand the ocean and climate response to uncertainties in discharge is by conducting modeling experiments. Climate modeling studies are critical in estimating or predicting future climate states, and how the earth system processes will change under human-induced climate change. Sensitivity studies provide insights on the relationship between various climate processes. Discharge is an important surface forcing for ocean components of global climate models (GCMs), or Earth System Models (ESMs). In a fully coupled ESM, discharge is simulated as an output of the land surface component of that ESM, and is susceptible to biases and inaccuracies in not only the land component, but in other components such as ocean, atmosphere, sea ice, as well as the method and frequency of coupling. This makes isolation and direct attribution of changes in ocean processes and properties to changes in discharge difficult in

a fully coupled ESM framework. However, if conducting experiments in uncoupled mode with only the ocean and sea ice components being active and coupled to each other, discharge forcing can be modified while keeping all other surface forcing same, thus enabling attribution of changes in the ocean variables directly to changes in discharge forcing.

In this study, we conduct a series of ocean-ice modeling experiments with varying discharge forcing to understand the response of the ocean to the changes and uncertainties in discharge forcing. By using the widely used COREv2 discharge forcing data based on *Dai et al.,* [2009], and the ensemble of reanalysis-based mass-balance estimates of discharge computed in the previous chapter, not only do these experiments offer a realistic insight on the discharge control of ocean processes, as opposed to more hypothetical 'hosing' studies, but also help to better quantify the biases in ocean models. The experiments help answer the following questions: 1. Which ocean processes and properties are sensitive to changes and uncertainties in discharge forcing? 2. What is the degree of the sensitivity? and 3. Which areas in global oceans are most sensitive?

In the next three sections, we provide details of the ocean-ice experiments conducted to answer the above questions. All the experiments are performed with Community Earth System Model (CESM) version 1.2 [*Gent et al.*, 2011; *Hurrell et al.*, 2013]. In all the experiments, CESM 1.2. is run in GIAF compset. In GIAF compset, the ocean and sea ice models are active and coupled together, while the model forcing from land and atmosphere is fed from COREv2 interannually varying forcing data. The ocean component of CESM is Parallel Ocean Program version 2 (POP2) [*Danabasoglu et al.*, 2012], and the sea ice component is Los Alamos sea ice Model version 4 (CICE4) [*Holland et al.*, 2012]. As mentioned earlier, the discharge forcing from COREv2 is based on *Dai et al.*, [2009] discharge, with added discharge from Antarctica

and Greenland. In all the following experiments, ocean-ice models are run at approximately 1° (gx1v6) resolution, with displaced pole grid. The control case for the experiments was based on COREv2 case CCSM4 g40.000, which can be downloaded from www.earthsystemgrid.org. The case has 5 reruns of 60-year (1948-2007) COREv2 forcing data. 4 cycles is considered as sufficient time for upper ocean model spin-up [*Griffies et al.*, 2012], and the last 60 years are usually used for analysis. Hence, the control case in this study was branched from the year 241.

3.2. Ocean sensitivity to interannual changes in discharge

3.2.1. Experiment design

As the Dai *et al.,* [2009] discharge is unavailable after 2006, COREv2 discharge after 2006 uses discharge climatology. In order to understand the sensitivity of the ocean to interannual variability (as opposed to climatology) in discharge, we force the ocean-ice components of CESM with climatological and interannual discharge forcing and analyze the model output.

We conduct two experiments: 1. a control run (henceforth referred to as 'GIAFc$_1$') with the discharge time series from 1948-2006, and 2. a sensitivity run (henceforth referred to as 'GCLIM') where the ocean-ice models are forced with monthly climatology of COREv2 discharge, repeated over 1948-2006. With other surface forcing data and model parameterization being the same, comparing upper ocean processes and properties between the two cases will help us understand the sensitivity to interannual forcing, and identify regions where the interannual variability in discharge plays an important role. We analyze the sea surface salinity (SSS) field in the model output, as SSS is strongly influenced by freshwater discharge.

3.2.2. Results and discussion

Figure 3.1 shows fraction of the standard deviation in SSS in the two cases, with numerator (denominator) in the fraction being GCLIM ($GIAFc_1$). Values less than 1 (Green and blue colors) indicate that the standard deviation has decreased when climatology was used; values equal to 1 indicate no change in variance; and values greater than 1 indicate increase in variance. As expected, no region in the global ocean shows increase in variance in SSS when discharge climatology was used for forcing. Open oceans show mild reduction in variance (0-10%). Plumes of several major rivers such as Amazon, Orinoco, Ganga, Brahmaputra, Yenisey, Lena, Ob, and Mackenzie show a moderate decrease (up to 30%) in variance. However, plumes of rivers Mississippi, La Plata, Columbia, St. Lawrence, Congo, Nile, Tigris and Euphrates, Changjiang, and Yellow show loss of variance by 50% or more.

Figure 3.1 shows the relative importance of interannual variability in the plumes of major river systems, and highlights the regions that will be most affected due to the lack of interannual variability in the COREv2 forcing since 2006. It should be noted that the loss of variance does not seem to be dependent on the discharge volume. For example, even though the discharge from Mississippi is much smaller than that from Amazon, the interannual variability in its discharge exerts a greater control on the SSS in its plume region compared to Amazon. The reason for the difference is likely due to several factors such as ocean depth, bottom topography, relative importance of the atmospheric freshwater fluxes (*E*-*P*), and surface advection and mixing.

3.3. Ocean response to realistic uncertainty in discharge forcing

In the previous section, we saw how using climatology instead of discharge time series, as is the case with COREv2 discharge forcing since 2006, influences ocean processes. In this

section, we provide an alternative to the discharge forcing to COREv2, based on the mass-balance estimates presented in Chapter 2. However, from Figure 2.2., it is evident that the discharge estimates from reanalysis-based *E-P* also have biases. How do these biases propagate as uncertainties in ocean fields? To understand this, we conduct similar experiments to Section 3.2 but this time, we force the ocean-ice model with ensemble of mass-balance estimates of discharge.

3.3.1. Experiment design

We run six cases of coupled ocean-sea ice models from CESM 1.2.2. The control case $GIAFc_2$ is branched from year 2004 from case g.e11_LENS.GECOIAF.T62_g16.009, which is a part of CESM Large Ensemble Project [*Kay et al.*, 2015], which receives the same discharge forcing as g40.000, but has up-to-date atmospheric forcing. The model configuration includes ocean ecosystem/biogeochemistry from the coupled Biogeochemical Elemental Cycling (BEC) Model [*Moore et al.*, 2004]. Each case is forced with identical atmospheric forcing for the 2004-2014 period. The first case is forced with the standard COREv2 discharge and serves as the control case ($GIAFc_2$), while each of the remaining five cases are forced with land mass-balance estimates of discharge from GRACE-based *dM/dt*, and precipitable water (*E-P*) from moisture convergences from five state of the art reanalysis data, viz. ERA-Interim ($GIAF_{ERA}$), JRA55 ($GIAF_{JRA}$), MERRA ($GIAF_{MERRA}$), MERRA2 ($GIAF_{MERRA2}$), and CFSR ($GIAF_{CFSR}$).

Analyzing the differences between the control and the sensitivity cases reveal the ocean's response to the differences between the COREv2 discharge compared to the mass-balance estimates of discharge and intercomparing the sensitivity cases reveals the ocean's response to the relative uncertainty among the mass-balance based discharge estimates. Given the short 10-

year simulation length, we limit our analysis to analyzing climatologies. The ocean properties that are analyzed are SSS, temperature, mixed layer depth (MLD), and stratification. Stratification is computed by taking the difference between the potential densities at surface and 200m depth following *Capotondi et al.*, [2012]. Active biogeochemistry enables computation of NPP, for which, carbon fixation rate by all three plankton functional types (diatoms, diazotrophs, and small phytoplankton) from the BEC monthly output files are integrated across the upper 150m depth.

3.3.2. Methods for discharge forcing data computation

The mass-balance components for each river basin are usually computed separately, then used in the mass-balance equation (equation 2.1) to solve for discharge. The result is a single time series for the entire basin. Using this approach removes spatial information, and equation 2.1. has to be solved separately for each basin. Thus, such an approach has limited usefulness as a discharge forcing dataset. Instead, we solve the mass-balance at each grid cell, so that discharge is computed at each grid cell, then we route it by using a river routing model. This way, the basin boundaries are implicitly respected by the surface topography information used in the routing scheme, discharge gets computed and routed globally, and yet it is possible to retain spatial information. It also enables a more direct comparison with gaged estimates because stations measure only the upstream part of the total basin discharge, while the basin masks for the mass-balance method typically cover the entire basin.

For discharge routing, the Catchment-based Macro-scale Floodplain (CaMa-Flood) model [*Yamazaki et al.*, 2011] was used. CaMa-Flood is a global scale hydrodynamic model that can run at high resolutions such as 0.25° x 0.25° resolution as used in this study, and enables

explicit parameterization of dynamics associated with sub-grid topography. Gridded runoff data from the mass-balance method for the period 2003-2014 were resampled at daily frequency, as required by CaMa-Flood. Runoff in Year 2003 was used to spin-up the model, and routed discharge from 2004-2014 was used for forcing.

Solving mass-balance at each grid cell is likely to introduce an error component in the computed discharge as *dM/dt* from the neighboring grid cells that could potentially influence discharge in real world, are ignored in this approach. This is more likely to be the case as the actual resolution of GRACE mascons is 3°x3° (even though the product is available at 0.5°x0.5°). However, this problem is likely to only affect small river basins, and the bordering grids or large basins. Also, accuracy of GRACE decreases over smaller basin areas (<200,000 km^2). Considering this, we selected 50 rivers after carefully considering their area and discharge volume. We computed discharge by both approaches (grid-scale solution of discharge, as well as basin averages), and except for Ganges-Brahmaputra, all the RMS error between the two discharge estimates were < 1 km^3/yr. Ganges-Brahmaputra showed RMS of 9 km^3/yr, which is still considerably less than its mean discharge of 890 km^3/yr.

Then, the discharge volumes from each of the 50 river basins in COREv2 discharge are replaced with mass-balance estimates for those river basins. Also, as the network map used in CaMa-Flood excludes the ice sheets, the default discharge from the ice sheets in COREv2 was scaled equally at each coastal grid cell such that the integrated discharge from each ice sheet will add up to the ice-sheet discharge estimates from mass-balance. Figure 3.2. shows the map of locations of grid-cells where COREv2 discharge were replaced by mass-balance estimates.

3.3.3. Results and discussion

Figures 3.3 – 3.7 provide mean differences between the climatologies of sensitivity runs and the control run for SSS, potential temperature at 50m, MLD, stratification, and NPP. It can be seen from Figure 3.3, that the mass-balance estimates of discharge generally freshen the coastal surface ocean, with highest freshening of up to 8 PSU occurring understandably near the river mouths. Almost all sensitivity cases show intense freshening near the Nile river mouth, and except for $GIAF_{JRA}$ and $GIAF_{ERA}$, at the Congo river mouth. $GIAF_{JRA}$ and $GIAF_{MERRA}$ also show mild positive salt anomaly in the Amazon plume, unlike other sensitivity runs. The increase in stratification (Figure 3.4) corresponds with the freshening signal seen in SSS. As stratification is computed using density differences at surface and 200m depth, coastal areas shallower than 200m, such as in the Arctic Ocean, are excluded in Figure 3.4.

Sea surface temperature (SST), being closely coupled with the atmospheric surface temperature, did not show a strong response to the changes in discharge forcing in the monthly model output. However, sub-surface temperatures still retain the signal due to changes in the discharge plume. Figure 3.5 shows the differences in potential temperature at 50m depth between sensitivity runs and the control run. The negative values (blue) indicate cooler temperatures in the sensitivity runs compared to $GIAFc_2$. All sensitivity runs show pronounced cooling by 3.2°C near the west coast of Africa north of Angola-Benguela front and south of equatorial SST front [*Meeuwis et al.*, 1990], and in the Levantine Sea, while warmer temperature can be seen in the Tyrrhenian Sea on the west coast of Italy, and in the northern Sea of Japan near the strait of Tartary. Further analysis will be needed to investigate if the temperature of the increased discharge would directly affect the temperatures in these plume regions. However, it is more likely that the temperature anomalies seen here are due to the changes in MLD. If the salinity-induced stratification from the added discharge shallows the MLD to be above 50m, then the

temperatures at 50m will be colder, while if the MLD that is already deeper than 50m is shoaled, but remains deeper than 50m, then the temperature at 50m will reflect the increase in temperature due to stratification.

Average MLD (Figure 3.6) is expectedly shoaled in most of the coastal regions with pronounced reductions (by more than 500m during winter) occurring in the southern coasts of Greenland (Labrador Sea and Denmark Strait) and Iceland, and southwest coast of Svalbard. South of the shoaled MLD in the Denmark Strait, there is a region of deepened MLD. The region coincides with a retroflected tongue of North Atlantic Current (NAC) carrying warm surface water. The shoaling of MLD (caused by increase in Greenland discharge) in the north of this tongue might inhibit mixing with NAC, which would then mix further south, thus creating a shoaled and deepened MLD front.

Salinity-induced stratification of the upper ocean due to increase in discharge would inhibit vertical mixing, reducing phytoplankton access to the nutrients, and thus cause a decrease in NPP. Expectedly, the overall NPP in the sensitivity runs (Figure 3.7) show a slight decrease in the Atlantic Ocean, Arctic Ocean, and along the coastal regions. However, plume regions of La Plata and Amur river show increases in NPP up to 15 $gC/m^2/yr$. As both these regions show decreases in the MLD (Figure 3.6), it is likely that the regions are light limited, hence shoaling of the mixed layer increases the NPP [*de Baar et al.*, 2005]. Average difference within the NPP from the ensemble of sensitivity runs and the control run over global ocean is -0.3 $gC/m^2/year$.

While Figures 3.3-3.7 highlight the differences between the control case and the sensitivity cases, Figure 3.8 highlights the differences within the sensitivity cases. The maps show the highest range (minimum – maximum values) within the ocean fields for each grid for any given month. If the mass-balance estimates of discharge were identical, the spread among

the ocean properties would be nil. Most regions show consistency with Figures 3.3-3.7, while some fields, where discharge estimates match well with each other, such as over Greenland, show less signal in SSS spread. Thus, depending on the reanalysis-based moisture convergences used for computing discharge, the spread among SSS, sub-surface temperature at 50m, MLD, and NPP, can be more than 4 PSU, 2°C, 50m, and up to 100 $gC/m^2/yr$ in the affected areas. The maximum spread among the sensitivity runs over the NPP adds an uncertainty of 0.4 Petagram of carbon per year over the global ocean.

3.4. Ice discharge from Antarctica

Ice sheets on Greenland and Antarctica continents serve as a large freshwater reserve on land. Over the ice sheets, mass input is snow precipitation, and mass is lost (from the grounded part of the ice sheet) through sublimation, wind drift, and discharge. Discharge estimates from ice sheets are sparely recorded, and little information about ice sheet discharge was available until recently. While discharge from Greenland is considered to be partly meltwater and partly ice discharge, discharge from Antarctica is believed to be primarily ice discharge due to severe cold temperatures in Antarctica [*Rignot et al.*, 2011a, 2011c]. However, the discharge from Antarctica is assumed to be completely liquid in COREv2 discharge forcing. How does this inaccuracy in Antarctic discharge forcing affect the ocean?

We use $GIAFc_1$ as the control case and conduct a sensitivity run $GIAF_a$ which is identical to $GIAFc_1$ except that the discharge from Antarctica is considered as ice discharge rather than liquid discharge.

Figure 3.9 shows the maximum difference in the climatological SST, and sea ice area between $GIAF_a$ and $GIAFc_1$ cases. SST show a general decrease around the Antarctic continent,

with up to 1.3°C in Prydz Bay in the eastern Antarctica. Decrease in SST is expected as the surface ocean loses heat in order to melt the ice discharge. Even though the discharge is uniformly applied all across the Antarctic coast, (i.e. it lacks spatial structure), the spatial signature in the response in SST indicates varying ocean dynamics. The added ice discharge also increases the sea ice extent by up to 20%. Almost all the differences among the two cases occur during Austral summer (December-February).

3.5. Conclusion

In this study we presented results from several ocean-ice experiments forced with varying discharge in order to highlight the sensitivity of upper ocean processes and properties to the changes in discharge forcing, and how uncertainties in discharge propagate into the upper ocean processes. We find that the loss of interannual variability in discharge, which is not captured in the post-2006 COREv2 forcing, is important for several major river plume regions, including the Mississippi, La Plata, Congo, Nile, Changjiang, and Yellow rivers. We showed how using mass-balance estimates instead of the COREv2, as well as differences within the mass-balance estimates, affect SSS, stratification, mixed layer depth (MLD), upper temperature at 50m, and NPP. Finally, we showed how Southern Ocean SST and Antarctic sea ice respond when correctly forced with ice discharge instead of liquid discharge from Antarctica.

This study highlights how our limitations in observing the global continental discharge affect our ability to correctly model upper ocean properties. The COREv2 framework was created in order to compare available global ocean-ice models with a common surface forcing, to complement the Coupled Model Intercomparison Project (CMIP). Thus, COREv2 have been used in many ocean-ice modeling studies. A model's skill at representing a field is typically

evaluated by comparing against observation. This study shows that in the river plume regions, a fraction of model-observation mismatch can be due to uncertainties associated with forcing data rather than model physics.

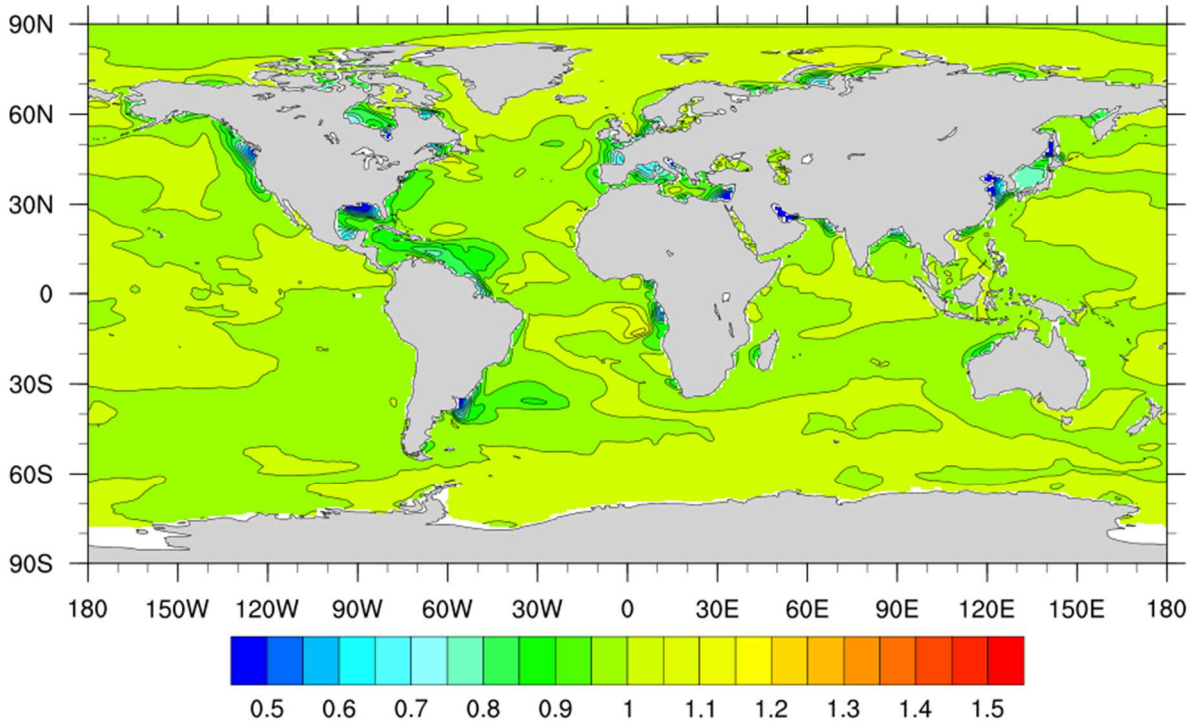


Figure 3.1. The fraction of standard deviation in sea surface salinity between the sensitivity case (GCLIM) and the control case ($GIAF_{c1}$).

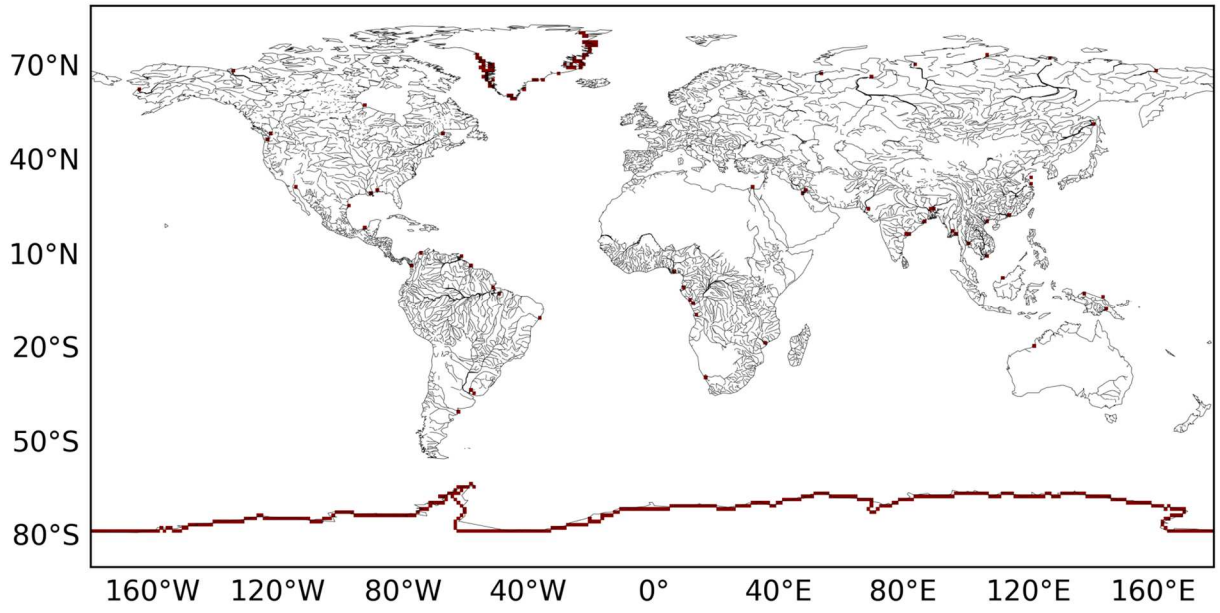


Figure 3.2. Map showing locations where COREv2 discharge data were replaced using mass-balance estimates of discharge.

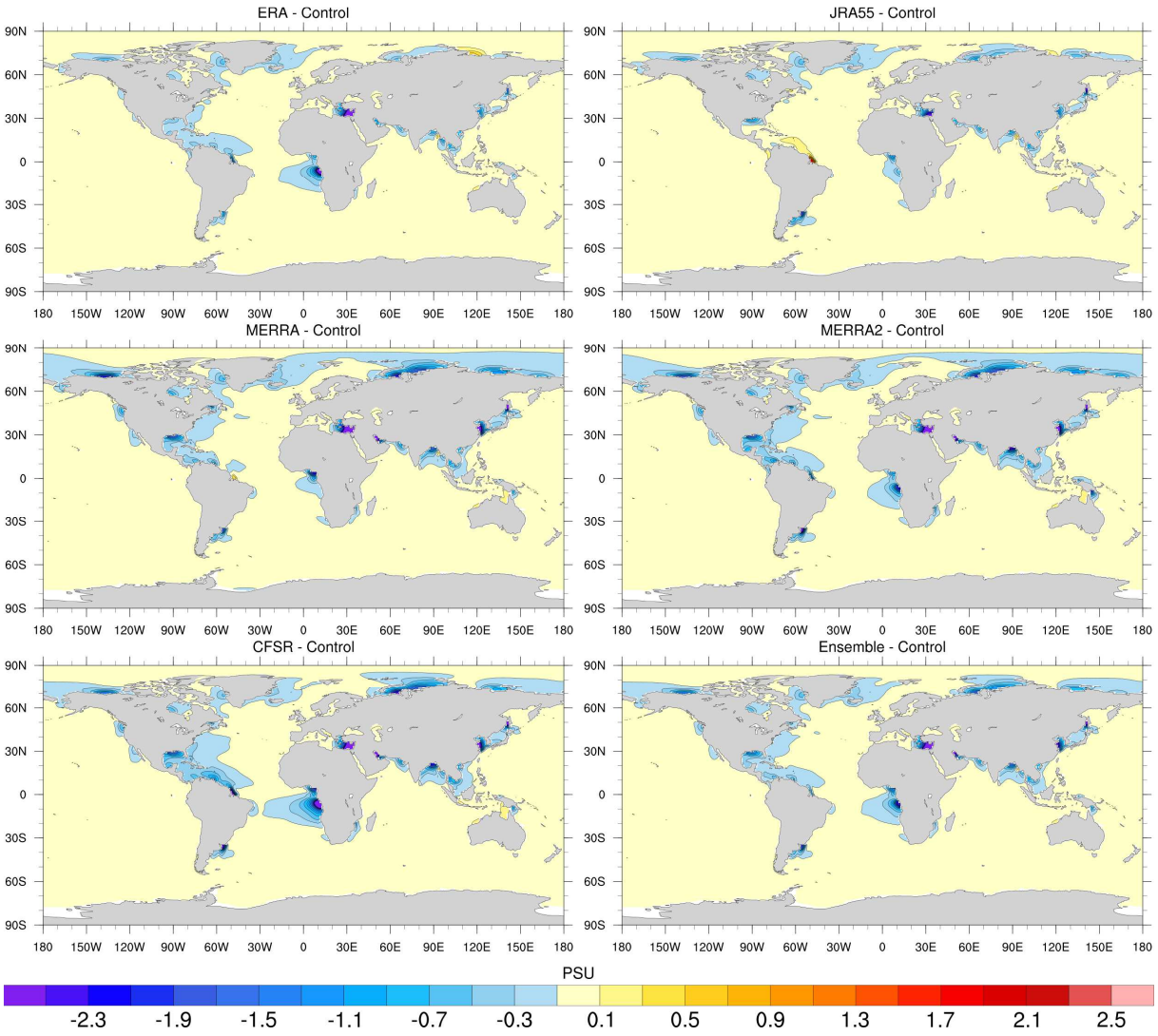


Figure 3.3. Mean difference in sea surface salinity from the monthly climatologies for the five sensitivity cases and the control case, and the mean ensemble of the sensitivity case and the control case (bottom right subplot).

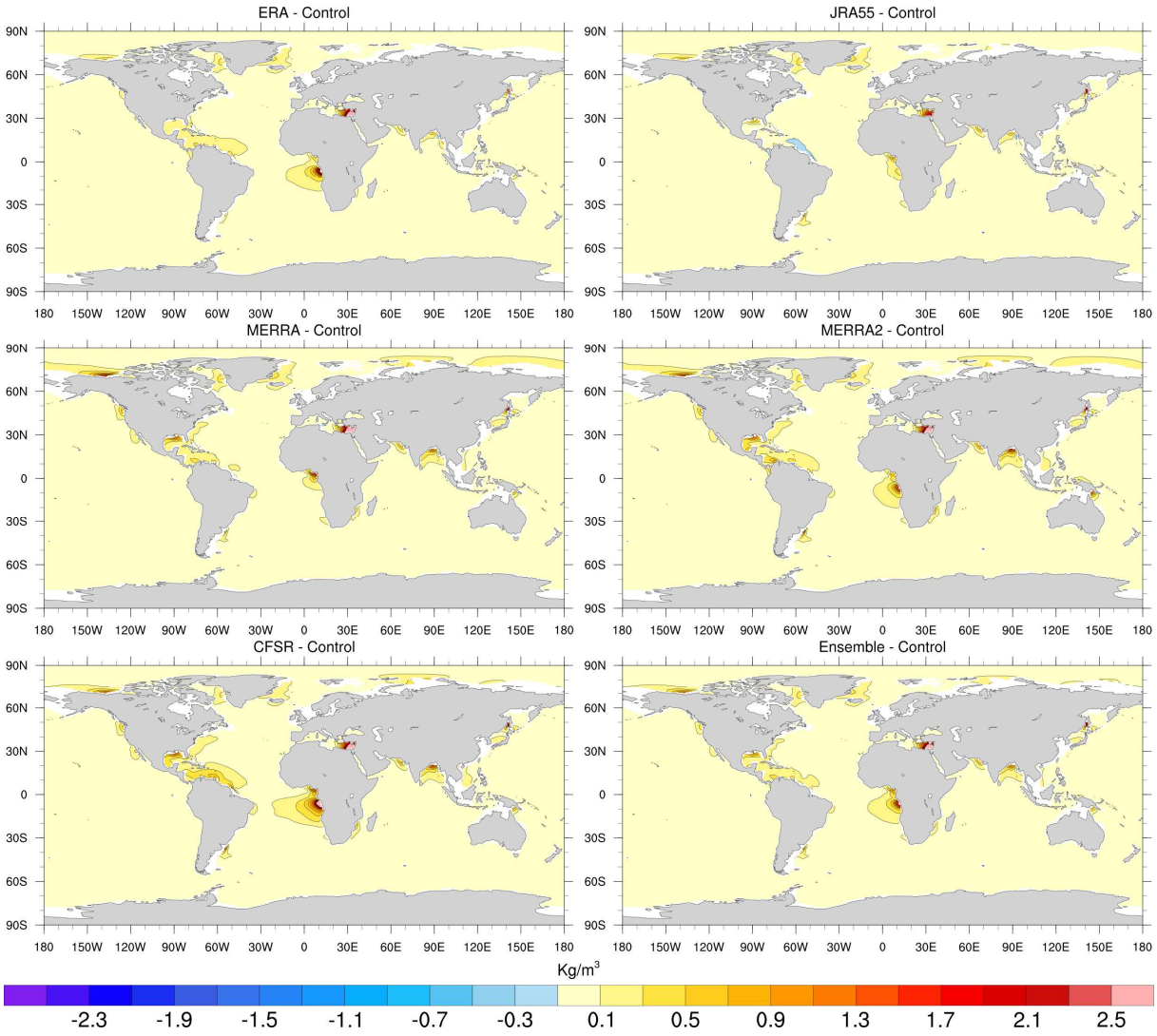


Figure 3.4. Mean difference in stratification from the monthly climatologies for the five sensitivity cases and the control case, and the mean ensemble of the sensitivity case and the control case (bottom right subplot).

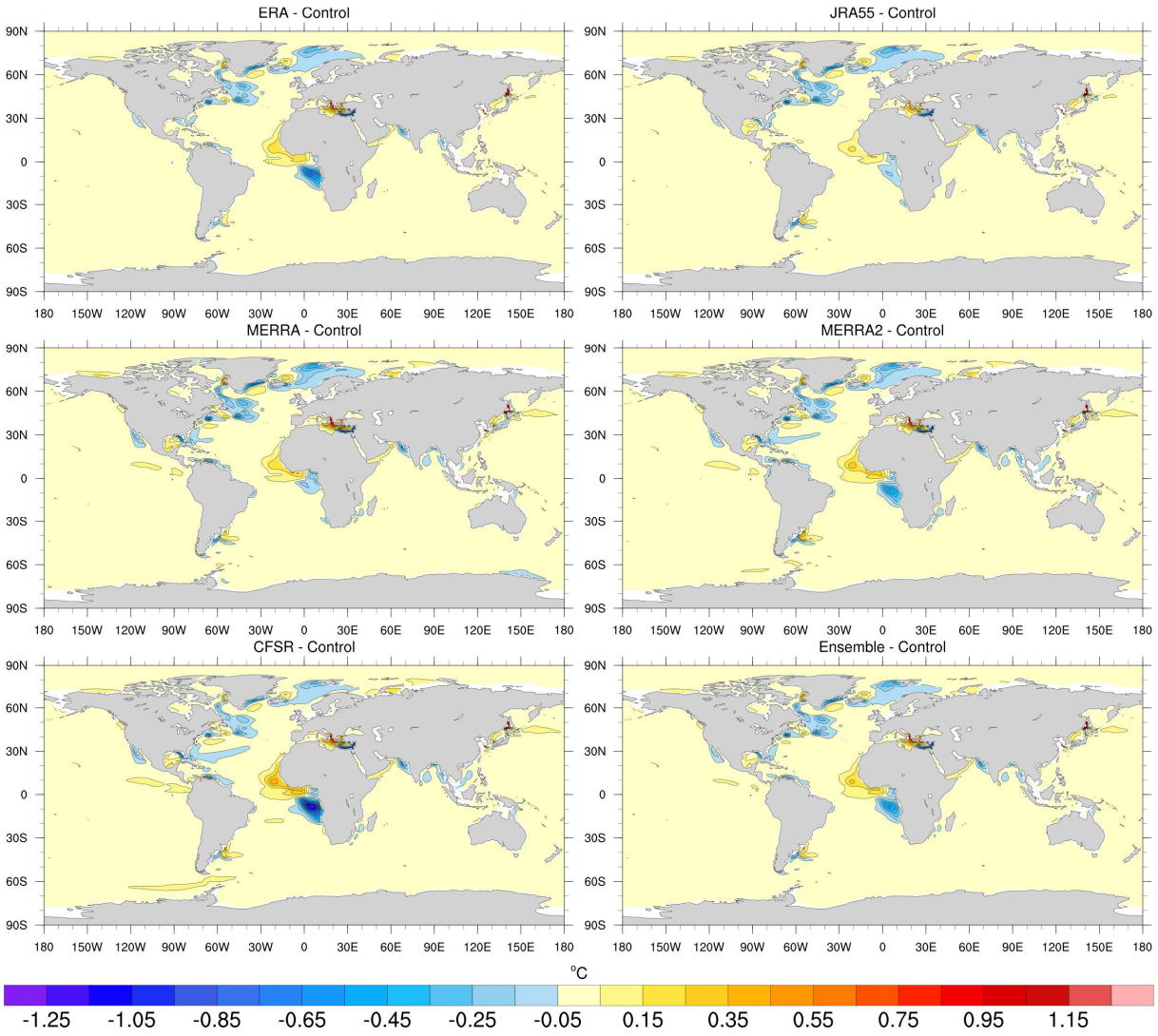


Figure 3.5. Mean difference in potential temperature at 50m, from the monthly climatologies for the five sensitivity cases and the control case, and the mean ensemble of the sensitivity case and the control case (bottom right subplot).

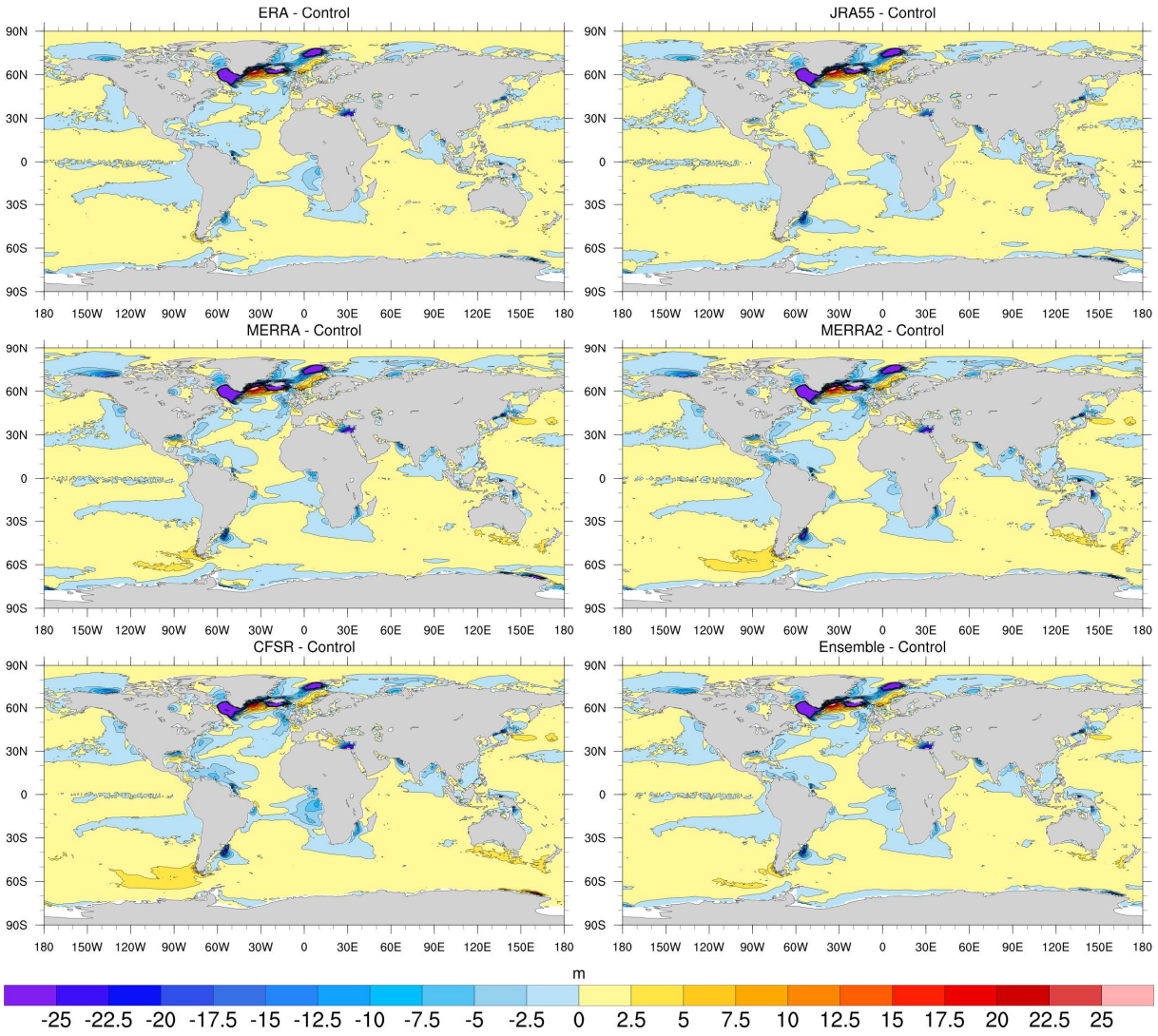


Figure 3.6. Mean difference in average mixed layer depth, from the monthly climatologies for the five sensitivity cases and the control case, and the mean ensemble of the sensitivity case and the control case (bottom right subplot).

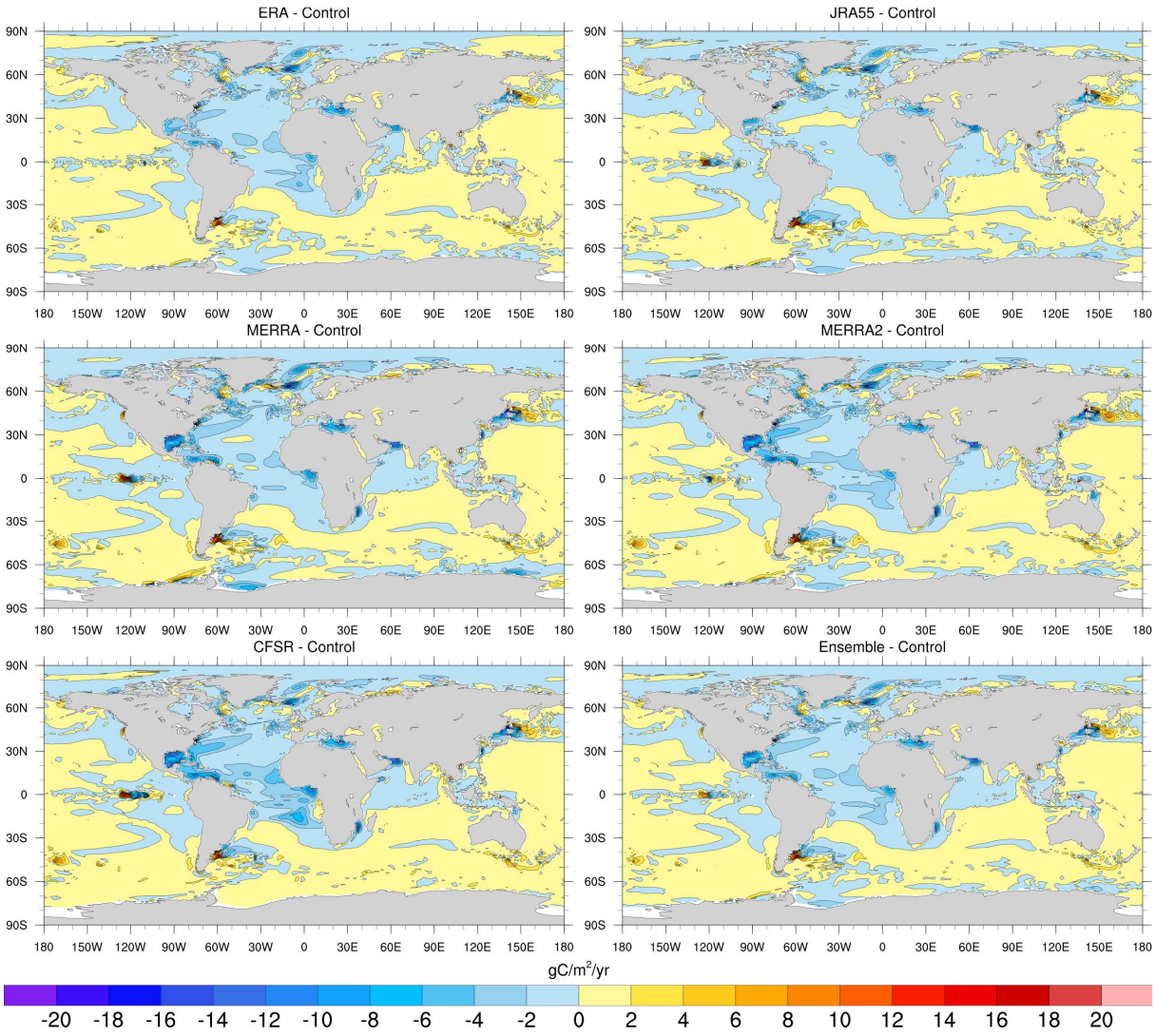


Figure 3.7. Mean difference in net primary production from the monthly climatologies for the five sensitivity cases and the control case, and the mean ensemble of the sensitivity case and the control case (bottom right subplot).

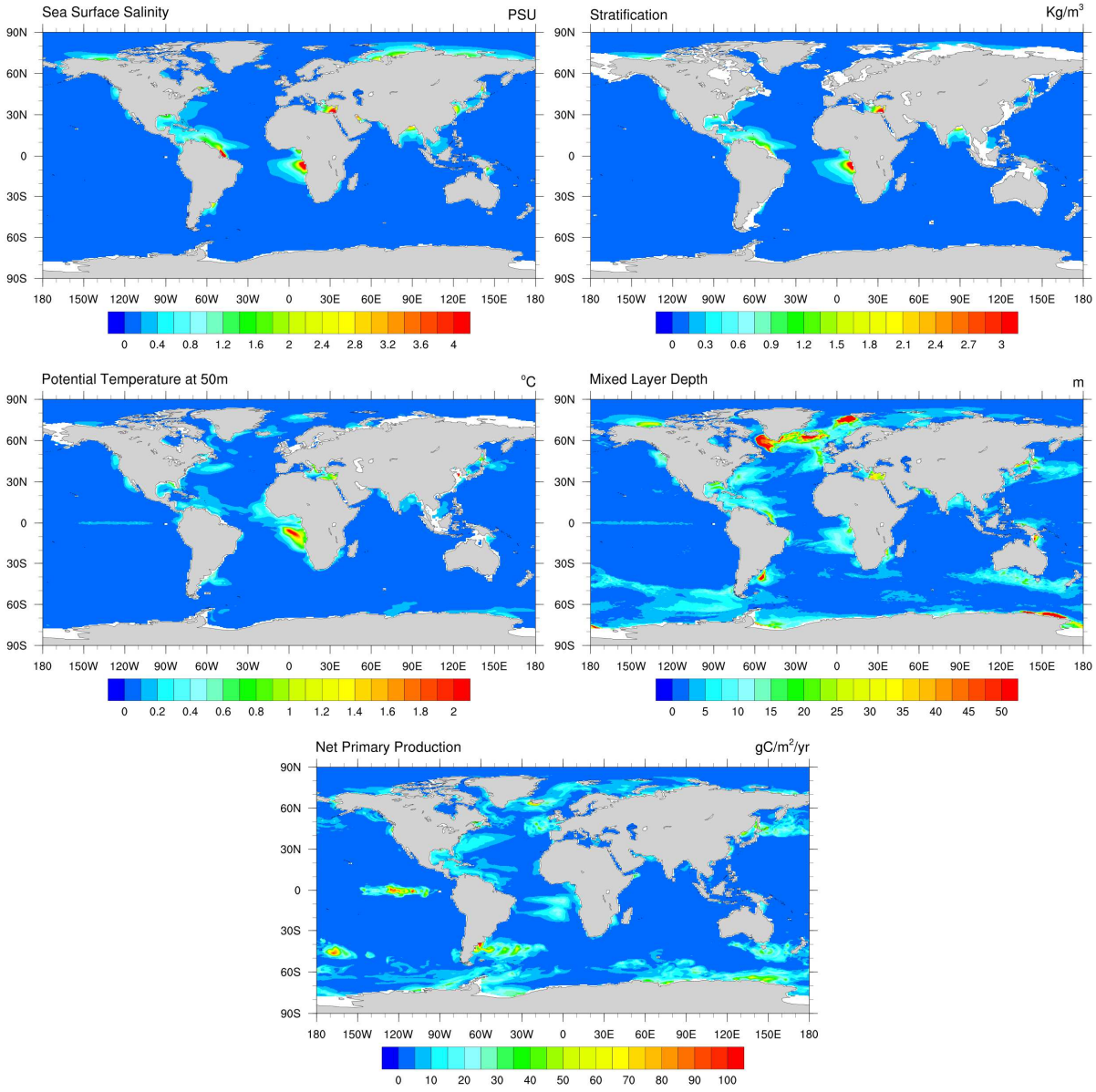


Figure 3.8. Maximum possible spread in the ocean fields among all the five sensitivity cases.

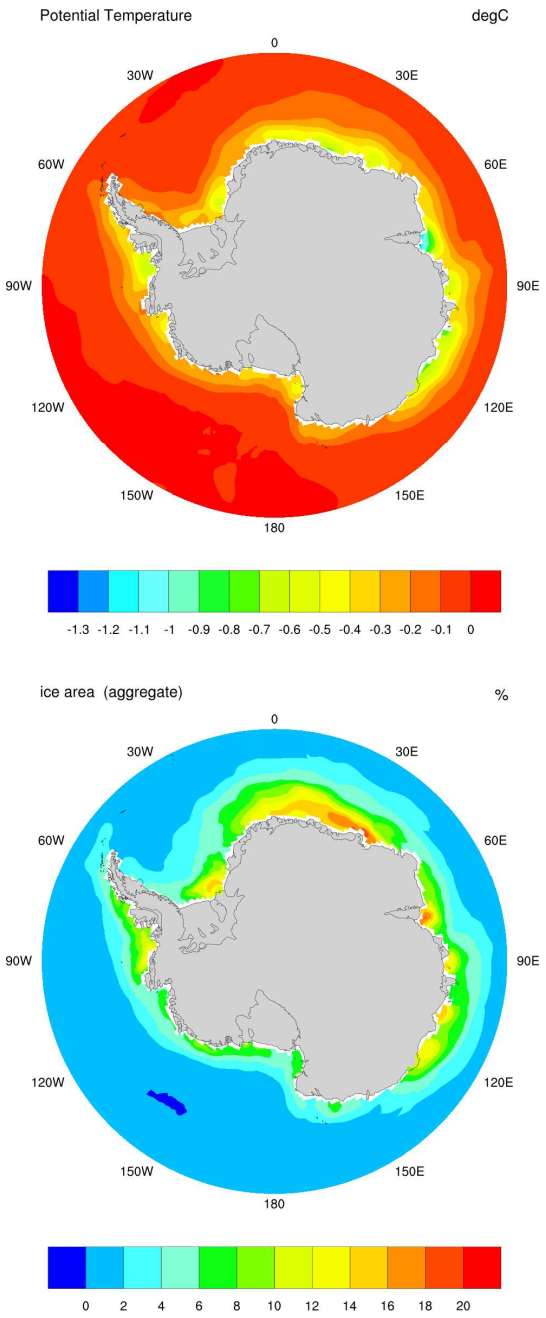


Figure 3.9. Maximum differences in sea surface temperature (top) and sea ice area (bottom) from the climatologies of $GIAF_a$ and $GIAFc_1$ cases.

Chapter 4

Continental discharge from Aquarius Sea Surface Salinity

Abstract. The mean distribution and variability of sea surface salinity (SSS) are governed by net differences between ocean evaporation and precipitation (E–P), continental discharge, advection, and subsurface mixing. In this study, Aquarius SSS observations are investigated to determine if variability in plume signatures from major river systems can be detected with sufficient skill to estimate continental discharge changes. We remove the influence of E–P by performing Joint Empirical Orthogonal Function (JEOF) analysis on E–P and SSS, and removing the dominant common mode and the temporal mean from the original SSS. The distribution of the resultant residual SSS anomalies corresponds with plume regions of major rivers. Examining the high-variability sections (top 1 percentile) of the residual SSS anomalies for three major plumes, we find that for plume regions whose high-variability sections are dominated by discharge, the discharge-SSS anomaly relationship can be used to estimate the discharge flux.

4.1. Introduction and Background

Freshwater discharge from the continents is a key flux in regional and global water cycles, yet is difficult to observe for many of the world's largest river systems [*Syed et al.*, 2005b]. A hypothetical alternative to land-based measurement of river flux would be an ocean-based detection system, but the complex dynamics of coastal freshwater plumes present several challenges. Plume regions are influenced by continental mass fluxes, atmospheric mass and energy fluxes, tides, surface winds, local currents, and bathymetry and as such are one of the most complex and dynamic regions in the ocean [*Sprintall and Tomczak*, 1992; *Fong and Geyer*, 2001; *Körtzinger*, 2003; *de Boyer Montégut et al.*, 2007; *Mignot et al.*, 2007; *Subramaniam et al.*, 2008]. Here we perform experimental analysis to test the hypothesis that a continental discharge signature can be detected in satellite ocean salinity observations with sufficient skill to quantify discharge volume.

In order to do this, we begin with the simplified mixed layer salinity budget, which can be written as:

$$\frac{\partial S}{\partial t} = \frac{F_w S}{h} + Transport \qquad (1)$$

where S is the mixed layer salinity (for which sea surface salinity (SSS) is a reasonable proxy); F_w is the net freshwater flux to the ocean from the imbalance between maritime evaporation, maritime precipitation, and continental discharge; *h* is the mixed layer depth; *Transport* represents ocean dynamics that include horizontal processes such as advection and the horizontal component of diffusion, and vertical processes such as entrainment and the vertical component of diffusion. Mixed layer salinity budget studies [e.g. *Dong et al.*, 2009; *Hasson et al.*, 2013; *Gao et al.*, 2014] provide valuable insights on the interplay of several processes in the upper ocean layer. However, understanding the relative importance of individual terms in such analyses

is difficult due to lack of observations and less-than-ideal fidelity of process representation in ocean models.

While the components of the transport term (especially the vertical component) in equation 1 are difficult to isolate and study without resorting to model-simulated estimates, observational data are available to enable isolation of the surface fluxes terms. The F_w forms an important term in the mixed layer salinity budget, and in river plume regions, continental freshwater fluxes usually comprise a significant fraction of this term. However, most mixed layer salinity budget studies do not explicitly include continental discharge in the F_w term, but account for it implicitly in the residual from the budget computation. This includes studies such as *Foltz and McPhaden*, [2008] and *Rao and Sivakumar*, [2003], which focus on river plume regions.

Several studies have related discharge dynamics with changes in SSS [*Gierach et al.*, 2013; *Hopkins et al.*, 2013; *Chaitanya et al.*, 2014; *Grodsky et al.*, 2014; *Reul et al.*, 2014]. However, to our knowledge, quantification and inference of discharge based on remotely sensed observations of SSS, precipitation (*P*), and evaporation (*E*) has not been successfully demonstrated for major rivers, likely due to contamination from the evaporation minus precipitation (*E–P*) and transport signals in SSS. For example, *Ibánhez et al.*, [2016] recently found that the Amazon plume extent is significantly overestimated due to precipitation-induced freshening at the Intertropical Convergence Zone (ITCZ).

In this study, we isolate and remove the atmospheric flux (*E–P*) signal from SSS variations in order to better characterize the importance of continental freshwater flux, along with transport, in SSS dynamics. We then explore whether the correlation between the resultant SSS anomalies and observed discharge variations can be used to reasonably infer discharge for major river systems.

4.2. Data and Methods

We use data from NASA's Aquarius/ SAC-D mission global sea surface salinity retrievals [*Le Vine et al.*, 2007] for the period 9/2011 - 5/2015 available at http://podaac.jpl.nasa.gov/. The data are Level 3, and are processed with JPL's Combined Active-Passive (CAP) V4 algorithm [*Yueh et al.*, 2014]. The algorithm applies a series of corrections to improve the brightness temperature observed by the Aquarius instrument, including correction for reflection of galactic and atmospheric radiation, the Faraday effect, and sea surface roughness. The algorithm also reduces the bias from ascending and descending passes to less than 0.1 PSS. According to *Yueh et al.*, [2014], the CAP data show an overall accuracy of about 0.2 PSS or smaller when compared to *in-situ* observations from Argo floats. The data are provided at spatial resolution of 1° x 1° latitude-longitude and at monthly frequency. While radio frequency interference (RFI) from highly populated coastal regions may affect SSS retrieval, RFI detection and mitigation algorithm works reasonably well [*Le Vine et al.*, 2014], and the data have been successfully used to study river plumes [*Gierach et al.*, 2013; *Grodsky et al.*, 2014; *Chao et al.*, 2015].

Global Precipitation Climatology Project (GPCP) Version 2.2 [*Adler et al.*, 2003] and CPC Merged Analysis of Precipitation (CMAP) [*Xie and Arkin*, 1997] data are used to represent maritime precipitation, and Objectively Analyzed air-sea Fluxes (OAFlux) [*Yu et al.*, 2008] are used to represent maritime evaporation. The two precipitation datasets are provided on 2.5°x 2.5° grids of global monthly mean precipitation, and are based on merging datasets from multiple satellites and inputs from *in-situ* observations. OAFlux data are 1° x 1° global grids of monthly

mean oceanic evaporation derived from merging satellite estimates, *in-situ* measurements of observable variables from Voluntary Observing Ships (VOS), and reanalysis products.

To account for potentially unquantified or unresolvable biases in the two precipitation estimates, the GPCP and CMAP datasets are first averaged together for each monthly grid to produce a common precipitation data. These data are then bi-linearly interpolated to 1° x 1° grids to achieve a similar resolution as the OAFlux data, multiplied by surface area of each grid to normalize for latitudinal differences, and are restricted to the oceans by using OAFlux as a reference to mask out land. All three datasets are then converted to common units of km^3/month. Finally, the combined precipitation estimate is subtracted from evaporation at each grid to obtain a gridded estimate of E–P.

We perform joint empirical orthogonal function analysis (JEOF) [*Bjornsson and Venegas*, 1997] on SSS and E–P data to reveal mutually unrelated (orthogonal) dominant modes of variability that are common to both SSS and E–P data, along with the fraction of total variability in the data explained by each mode. The two fields are first normalized, and then appended into a large dataset. The temporal mean of the data is removed to give an anomaly matrix $A_{(time,\ location)}$. Then singular value decomposition (SVD) is performed such that:

$$svd(A) = U\Sigma V^T \qquad (2)$$

where U gives eigenvectors (EOFs), which are spatial maps of each mode; Σ^2 gives eigenvalues, which represent the fraction of total variance explained by each mode; and V gives principal components (PC), which are time series showing the amplitude and frequency of each mode. Outputs of the JEOF analysis include the EOF, eigenvalue, and PC for each mode of the combined dataset, as well as the EOFs for each of the two sections (representing the two variables) of the combined dataset.

Based on *North et al.*, [1982], only those eigenvalues whose distance from the neighboring eigenvalue is greater than the sampling error are selected. Sampling error associated with each eigenvalue λ is $\delta\lambda = \lambda\sqrt{2/N}$ where N is the total number of eigenvalues needed to explain the entire variability of the input data. We also perform individual EOF analysis of SSS as well as *E–P* for comparison with the JEOFs.

The dominant modes obtained from JEOF analysis between SSS and *E–P* contain most of the variability that is common between the two fields. SSS is reconstructed by projecting the PCs of these modes onto corresponding EOFs of the SSS part of the appended dataset. Removing this reconstructed SSS and the long-term mean Aquarius SSS from the Aquarius SSS fields yields residual SSS anomalies that are devoid of the dominant patterns that are common with *E–P*. Thus, variability in these residual SSS anomalies is primarily associated with non-*E–P* processes such as discharge and transport. After computing the monthly climatology, we describe the seasonal dynamics of these SSS anomalies.

As data frequency affects the outcome of EOF analysis, we only include those grid cells that have more than 50% of the data for each year under consideration, and consider only modes with annual to interannual frequencies. Thus, high latitude areas with varying sea ice, including the plume regions of all major rivers flowing into the Arctic Ocean, are excluded. Also, while joint EOF analysis enables separation of common modes between *E–P* and SSS, it also removes the fraction of the discharge signature that is highly correlated with *E–P*. Thus, the amplitude of the SSS anomalies in the river plume regions is a conservative estimate.

4.3. Results and Discussion

4.3.1. Removal of *E–P* signal from SSS

Figure 4.1 (top) shows long-term mean distributions of SSS (from Aquarius), and *E–P* (from arithmetic averages of GPCP and CMAP, and OAFlux data). The colors in the figure represent SSS, while the dashed contour separates areas of $(E–P) > 0$ from those where $(E–P) < 0$. Both SSS and E–P show higher values (positive *E–P*) in subtropical gyres and lower values (negative *E–P*) in the ITCZ belt and higher latitudes. However, the mean variability (standard deviation) of SSS, as shown in Figure 4.1 (bottom), predominantly highlights locations containing plumes of world's major rivers such as the Amazon, La Plata, Mississippi, Mackenzie, Congo, Niger, Ganga, Brahmaputra, Irrawaddy, Changjiang, Yellow, Amur, Lena, Yensei, and the Ob. Oceanic transport signals in the Greenland Sea (likely associated with sea ice export from the Fram Strait), the north Indian Ocean, and the equatorial Pacific [*Alory et al.*, 2012; *Yu*, 2014] are also seen. It is evident from Figure 4.1 that the variability in SSS, at least at monthly timescales, is likely to be governed by continental discharge and oceanic transport.

Figure 4.2 shows the outputs from the JEOF analysis including, 1st JEOF maps of the SSS and *E–P* sections of the combined matrix along with superimposed contours of the respective 1st EOFs of the *E–P* and SSS fields from individual EOF analyses; the 1st PCs of JEOF and individual EOF analysis; and the fraction of the total variance explained by each mode along with the associated sampling error. The 1st mode of JEOF analysis explains 60 % of the total variance observed in the combined normalized SSS and *E–P* anomaly matrix, and, based on sampling errors, separates significantly from the rest of the modes. The 1st PC of the JEOF correlates very well with those from individual EOF of SSS and *E–P* (R = 0.8 and 0.9, respectively) suggesting that all three modes represent the same physical drivers of variability. The 1st PC of SSS lags behind that of *E–P* by 2-3 months. This lag is understandable considering *E–P*'s relation to SSS tendency (as opposed to SSS) in equation 1.

4.3.2. Seasonal dynamics of major river plumes

As most of the *E–P* signal is removed from the SSS during JEOF analysis, the residual SSS anomalies enable observation of the discharge- and transport- influences on the dynamics of major river plumes. The climatological annual cycle of these anomalies is shown in Figure 4.3 (Amazon-Orinoco, Congo-Niger, Mississippi, and La Plata), and Figure 4.4 (Ganges-Brahmaputra-Irrawaddy, and Changjiang-Yellow). Negative (positive) anomalies as represented in blue (red) indicate freshening (increase in salinity). The arrows represent monthly climatologies of surface circulation from the OSCAR (Ocean Surface Current Analysis Real-time) dataset [*Bonjean and Lagerloef*, 2002] for the Aquarius period.

The Amazon-Orinoco plume shows freshening anomalies starting in March through August. The plume spreads north and northwest due to the North Brazilian Current (NBC) before retroflecting in June and feeding into the North Equatorial Counter Current (NECC) [*Hellweger and Gordon*, 2002]. From August onwards, positive salinity anomalies start developing as the low salinity plume areas get displaced by relatively saltier water due to circulation and mixing and continue to grow until February. Similarly, the seasonality of the Mississippi River plume can be seen with freshening anomalies from May to August and following a relatively stronger southwest current in August. From September onwards the plume gets diluted by advection and mixing in the Gulf of Mexico, and positive salinity anomalies increase in intensity as discharge recedes. The plume of River La Plata also shows seasonal freshening (October through February) and positive salinity anomalies (March through September).

The residual SSS anomalies also successfully show the bimodal discharge of the Congo River. The Congo crosses the equator twice, and due to the seasonal shift in the ITCZ, receives

rainfall throughout the year [*Lee et al.*, 2011], and hence shows bimodal discharge [*Campbell*, 2005; *Labat et al.*, 2005; *Hopkins et al.*, 2013]. Freshening anomalies can be seen at the river mouth in October-January, and then again in March-May, corresponding to the two discharge peaks, while positive anomalies in June-September correspond with the low discharge period. The plume can be seen progressively moving south along the coast due to Angola Current from January-May and then spread west due to Benguela Current. River Niger shows a relatively clear seasonality with freshening from October till February followed by positive anomalies from March till September.

Plume dynamics in Bay of Bengal are governed primarily by the East Indian Coastal Current (EICC) which flows northeast along the eastern coastline of India during summer and reverses to flow southwest during winter [*Akhil et al.*, 2014]. Freshening anomalies beginning August at the mouth of Ganges-Brahmaputra (GB), and September at the mouth of Irrawaddy progressively move west along the coast of India and Sri Lanka, and into Arabian Sea. Reversal of EICC February onwards results in positive anomalies that continue till July. Seasonality of Changjiang-Yellow plume in the East China Sea can also be observed with freshening anomalies from May through August followed by positive anomalies. However, several grid cells of the plume along the coast were excluded from the EOF analysis due to temporal inconsistency. As a result, the plume shows a somewhat muted signal compared to the Bay of Bengal plume.

4.3.3. Discharge estimation from the residual SSS anomalies

In order to detect the river discharge signal in the residual SSS anomalies, we further restrict the analysis to regions with high variability in SSS anomalies. For this, we first compute the range (maximum - minimum) of the SSS anomaly values encountered at each ocean grid

point. This is shown in Figure 4.5 (top) as color shading. We then select only those grid cells with a range higher than the 99th percentile, as shown by the blue contour in the figure. As can be seen from the figure, most of the grid cells selected belong to the plume regions of major river systems. Catchment basin boundaries of the rivers Amazon, Orinoco, La Plata, Mississippi, Congo, Niger, Brahmaputra, Ganga, Irawaddy, Changjiang, Yellow are shown in a brown outline.

From these river systems, we analyze the discharge-plume relationship for Amazon-Orinoco, Congo-Niger, and Mississippi river systems, as discharge observations for overlapping duration with the Aquarius data are available for these rivers at gaging stations at Obidos (Amazon), Ciudad Bolivar (Orinoco), Beach Brazzaville (Congo), and Baton Rouge (Mississippi). Though discharge is not available for Niger, the mean discharge is much less compared to Congo and is well correlated, hence including it is not likely to significantly alter our results.

Observed discharge shows excellent anti-correlation (R= -0.9) with the spatially averaged residual SSS anomalies for both Amazon-Orinoco and Congo-Niger, but poor correlation (0.2) for Mississippi plume sections. Using a simple linear regression model based on the first 24 months of Aquarius data, we estimate discharge for the rest of the time series. Figure 4.5 (bottom) shows observed discharge (black), regressed discharge (blue) for the first 24 months which is used to train the model, and predicted discharge (red) for Amazon-Orinoco and Congo-Niger plume sections. A higher coefficient of determination value between the SSS anomalies and discharge observations for these river systems (R^2 is 0.8 for both), indicates a minimal contribution from oceanic transport to the residual anomalies for these plumes, whereas a poor

discharge-plume relationship for the Mississippi indicates a major contribution of transport to the high-variability plume sections, also observed by [*Fournier et al.*, 2016].

As we consider only the 1st mode of JEOF analysis (Figure 4.2), the residual SSS anomalies are likely to have some signal from E–P belonging to the later - though much less dominant - modes. We estimate uncertainty introduced by these signals as the mean spread among the residual SSS anomalies (color shading in Figure 4.5(top)) which is 0.4 PSS. This is much lower than the mean spread among the high-variability regions (areas within the blue contour in Figure 4.5 (top)) which is 4.7 PSS. Thus, the uncertainty in our method is unlikely to affect the prediction skill for the plumes we analyzed.

4.4. Conclusion

In this study, we test a hypothesis that a continental river discharge signature can be detected in satellite ocean salinity observations with sufficient skill to quantify discharge volume. After removing the *E–P* signal from SSS (with 0.4 PSS uncertainty) by removing the common dominant mode between *E–P* and SSS fields using JEOF analysis, the residual SSS anomalies show pronounced signatures from river discharge and transport. From the SSS anomalies, we select those plume sections that show very high variability (top 1 percentile), and compare the spatially averaged SSS anomaly in those sections with observed discharge. We find that for plume regions whose high-variability sections are dominated by discharge, the discharge-SSS anomaly relationship can be used to estimate discharge flux. This method is particularly useful for gap-filling discharge data, such as temporal gaps in observed discharge time series (black) in Figure 4.5 (bottom). It may also be useful for monitoring changes in discharge from large river systems where observations are not readily accessible, and in

understanding the role of river discharge in the freshwater flux around the continental margins. In well-gauged basins, this method may also provide insight on the subsurface component of the basin discharge.

4.5. Acknowledgments

We are grateful to University of California Office of the President Multicampus Research Programs and Initiatives and the NASA IDS Sea Level program for supporting this research. The datasets used in this study were acquired from the following sources. Aquarius: http://podaac.jpl.nasa.gov/; GPCP and CMAP: http://www.esrl.noaa.gov; OAFlux: ftp://ftp.whoi.edu; OSCAR: http://podaac.jpl.nasa.gov/. A portion of this work was conducted at the Jet Propulsion Laboratory, California Institute of Technology, under contract with NASA.

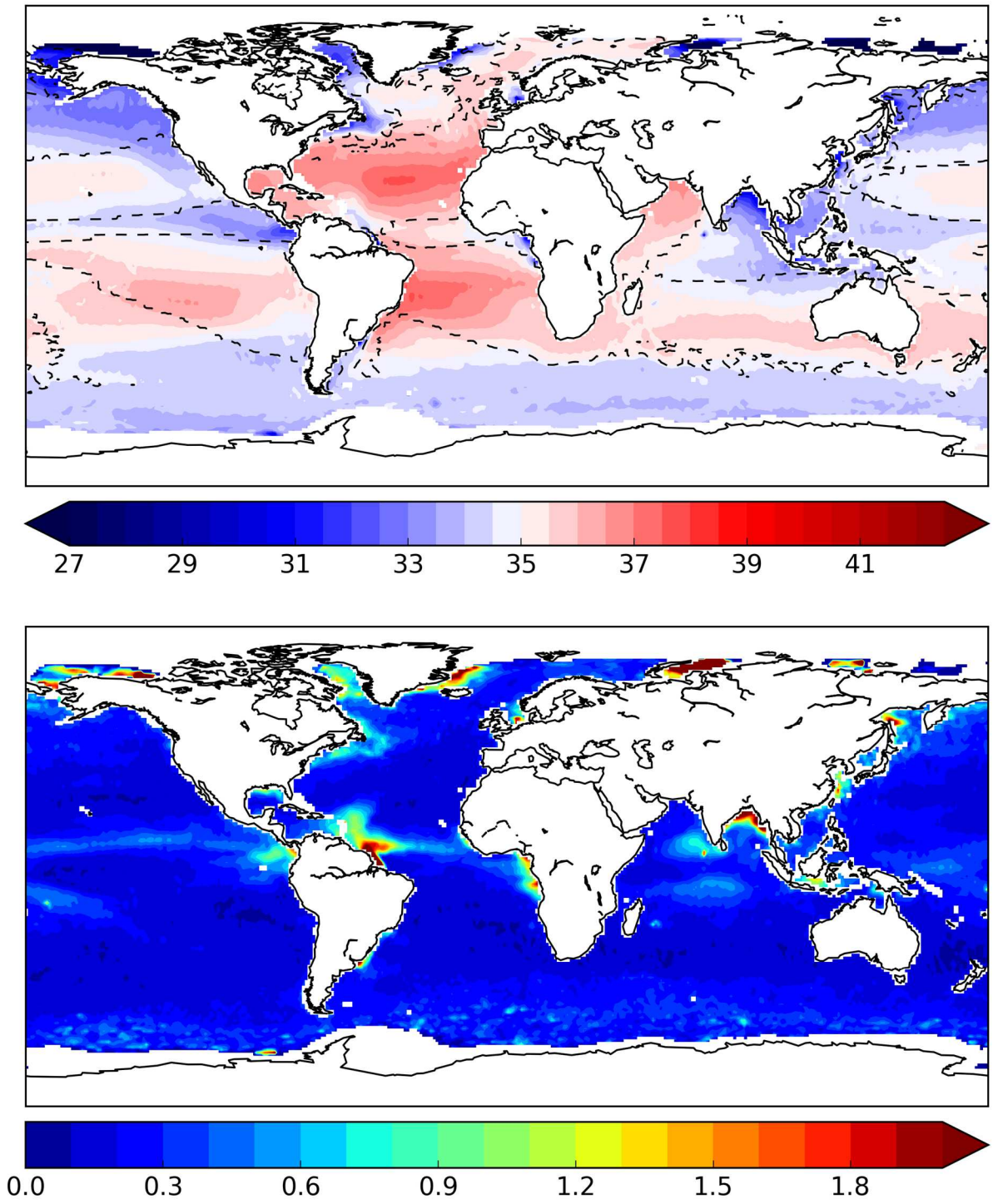


Figure 4.1. (top) Long-term mean distribution of SSS (color shading, units: PSS) and E–P (contour map, units: km^3/month). Dashed contour indicates (E–P) = 0. (bottom) Long-term standard deviation of SSS (units: PSS).

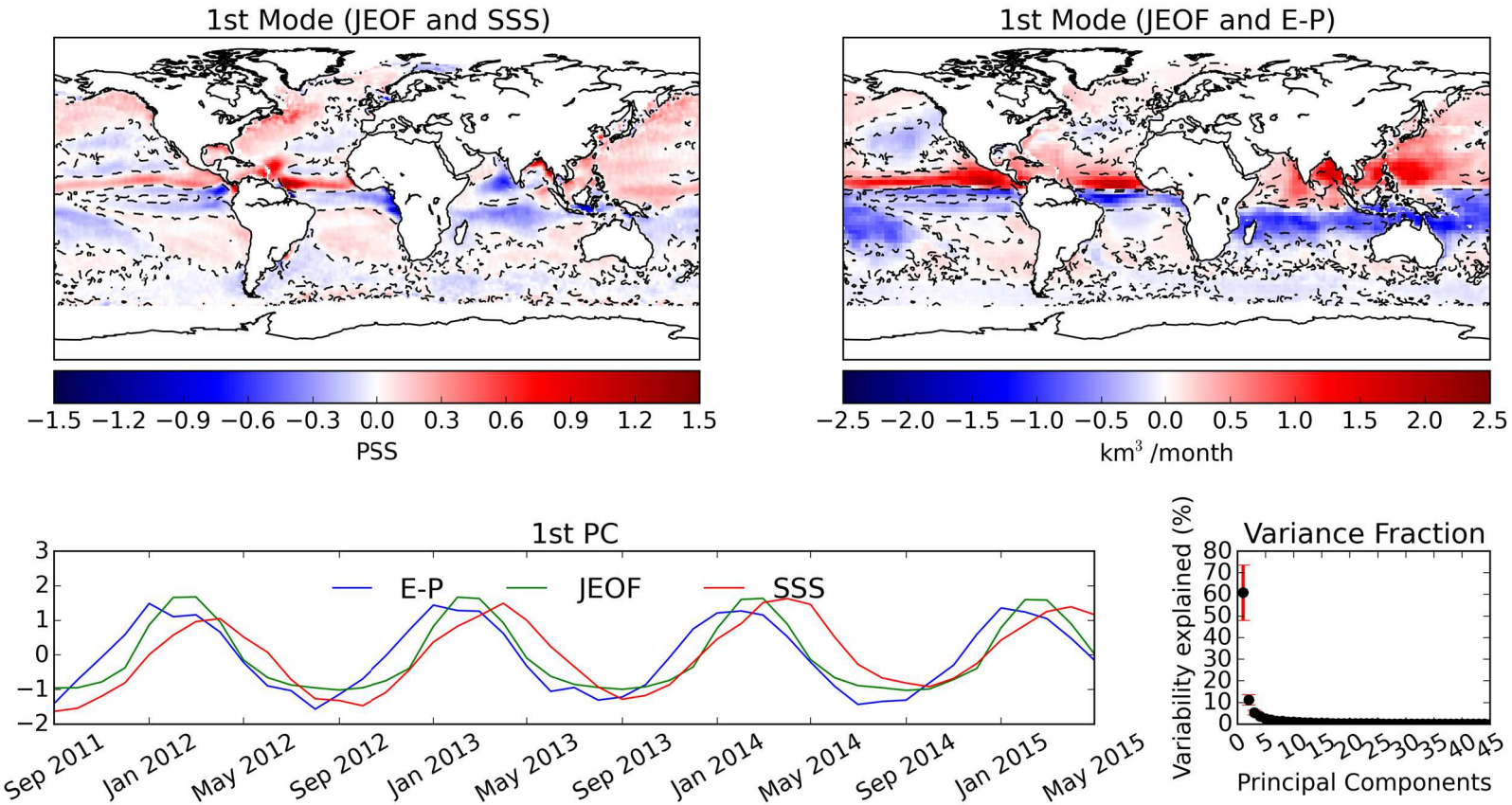


Figure 4.2. Joint EOF analysis of Aquarius SSS and ocean E–P showing 1) 1st JEOF maps (color shading) of E–P and SSS, superimposed with 1st mode individual EOF maps (contours), 2) Principal component of 1st mode of joint EOF as well as individual EOF of SSS and E–P, and 3) Fraction of the total variance (in %) explained by each mode along with associated sampling error.

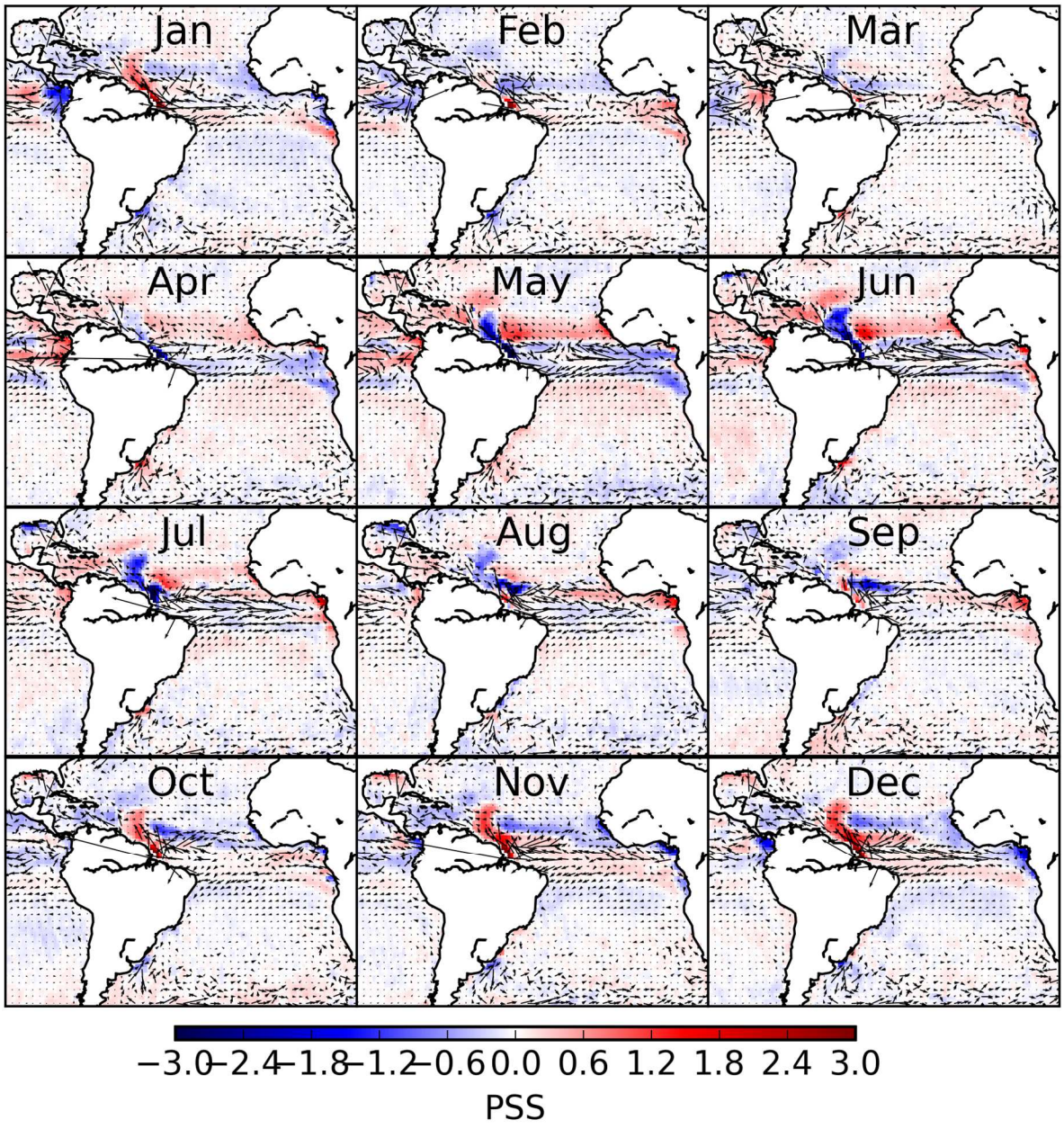


Figure 4.3. Monthly climatological maps of the residual SSS anomalies highlighting plumes of Amazon-Orinoco, Mississippi, La Plata, and Congo-Niger. Arrows represent monthly climatologies of surface circulation.

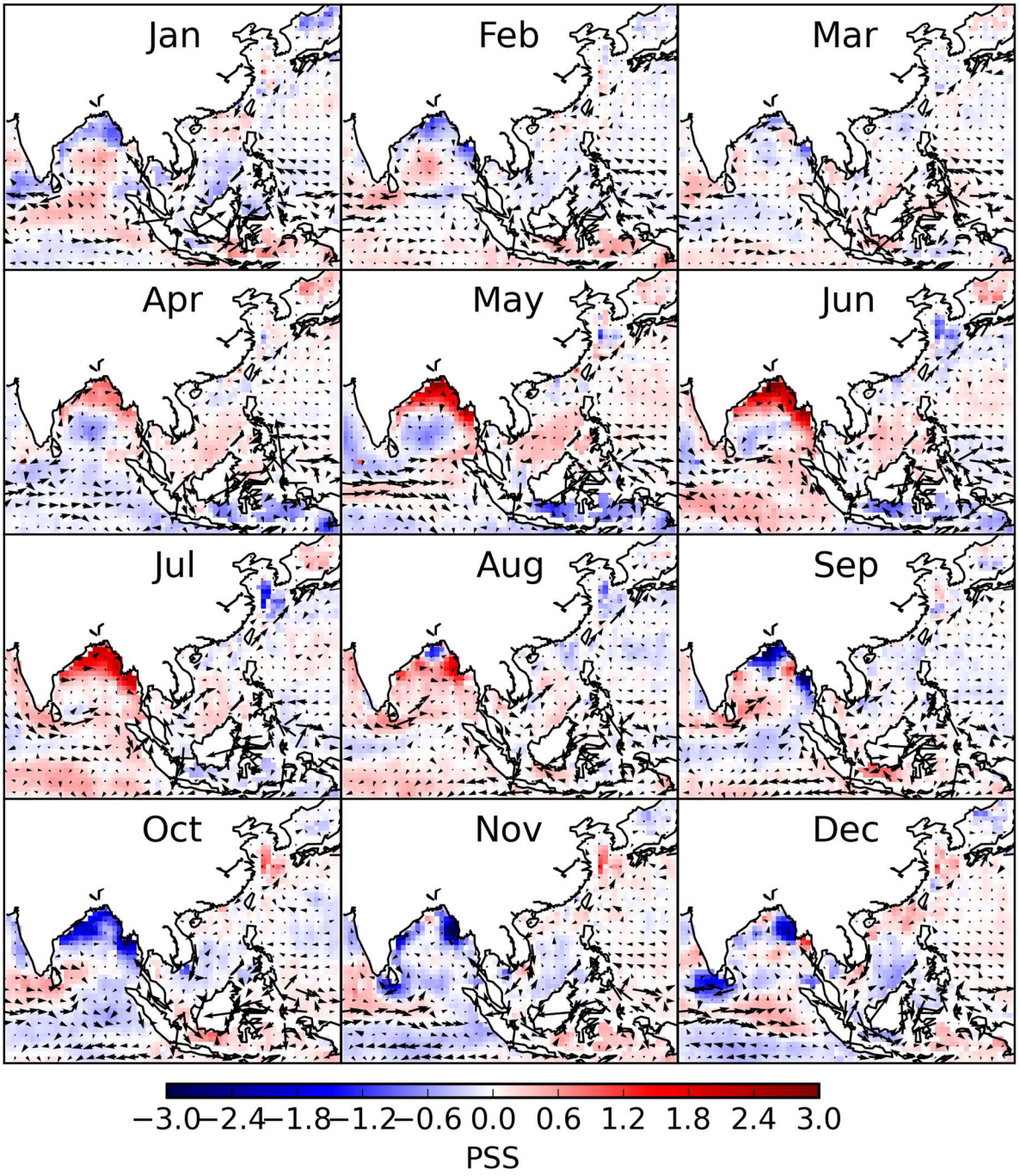


Figure 4.4. Same as Figure 4.3, but for plumes of Ganga-Brahmaputra-Irrawaddy, and Yangtze-Yellow.

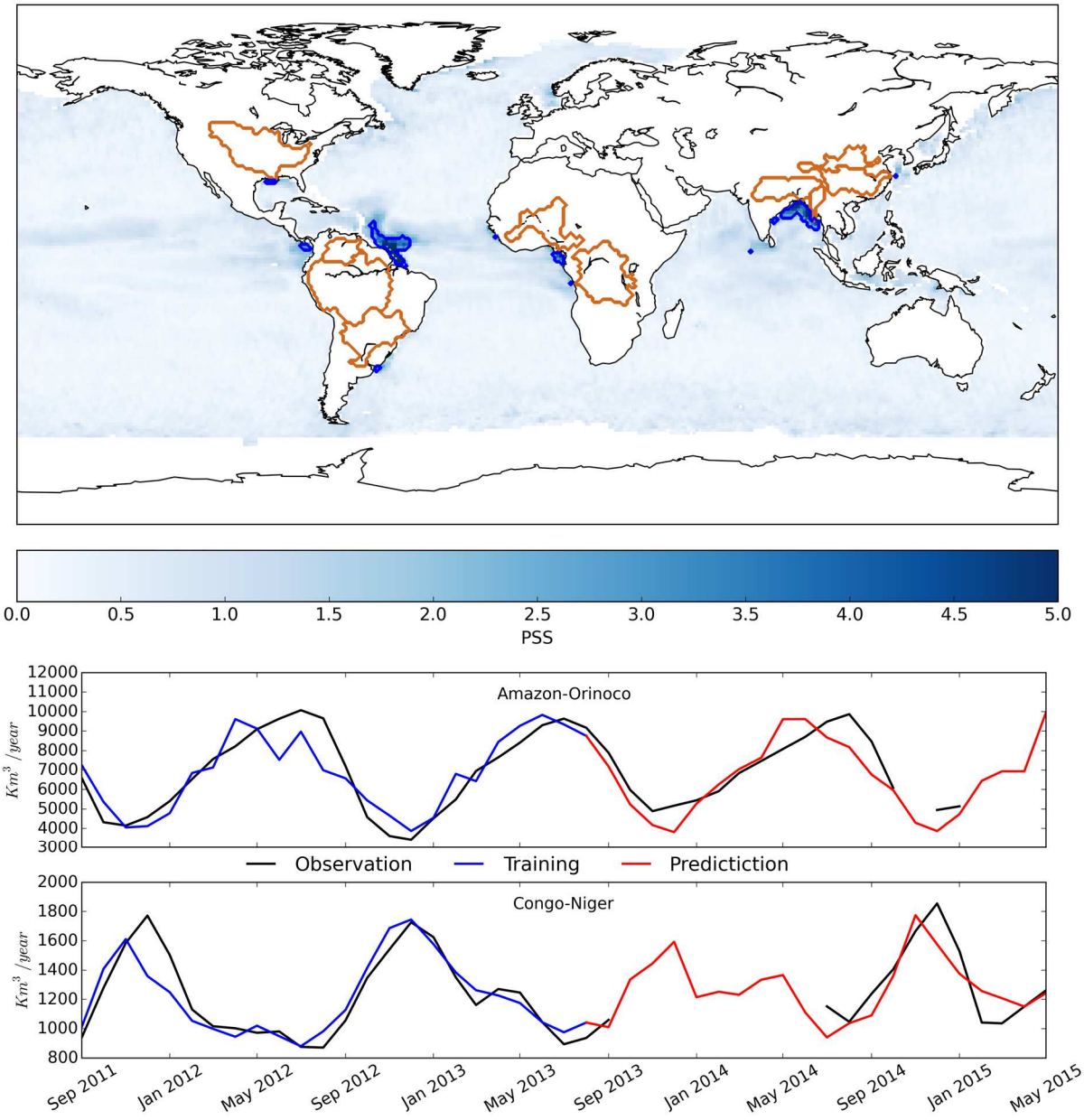


Figure 4.5. (top) Total spread of values (maximum - minimum) at each grid of the residual SSS anomalies (color shading, units: PSS) obtained after removing the 1st mode of JEOF and the long-term mean from Aquarius SSS data. Blue contour marks the 99th percentile of the range in the SSS anomalies. Marked brown are basin boundaries of major river basins. (bottom) Time series of observed discharge (black), modeled discharge over training period (blue), and over prediction period (red) for Amazon-Orinoco and Congo-Niger basins.

Chapter 5

Conclusion

5.1. Summary of Results

In this dissertation, we reviewed our ability to measure global continental discharge, and conduct ocean-ice modeling experiments to test the sensitivity of the ocean to changes and uncertainties in discharge.

In Chapter 2, we provided an overview of current observation systems of global discharge. We also presented our own complimentary estimates of discharge by solving water mass balance over land and ocean. We find that water mass change component (*dM/dt*) over land and ocean is well constrained, as we get very good agreement between ocean altimetry-based *dM/dt* after removing steric signal from upper 2000m of ocean, and direct mass anomalies (and subsequent derivative) measurements from GRACE. The most pressing challenge in computing mass-balance estimates of discharge is the atmospheric freshwater flux (*E-P*) term. By comparing multiple products for *P*, *E*, and *E-P*, we get a wide range of estimates of *E-P*. From these, we use observation-model hybrid data to further refine our estimates, and conclude that moisture convergence estimates from reanalysis provide better agreement with observations.

In Chapter 3, we examined output from several ocean-sea ice model experiments in order to understand ocean sensitivity to changes and uncertainties in discharge forcing. We first analyzed how using discharge climatology as opposed to interannually varying discharge affect the oceans. We find several major river basins show loss of variance in SSS. Then we replace the default discharge forcing mass-balance estimates from Chapter 2 for 50 major rivers, and observe changes in SSS, stratification, potential temperature at 50m, MLD, and NPP, particularly in the coastal and river plume regions. Finally, we replace the default liquid discharge from

Antarctica with ice discharge, and observe decrease of up to 1.5°C in austral summer SST, along with up to 20% increase in sea ice area.

In Chapter 4, we use the discharge-SSS relationship to infer discharge from SSS observations after removing *E-P* fluxes from the atmosphere using joint EOF analysis. Comparing the high variability regions in the resultant SSS anomalies with observed discharge for three major river systems, we find that for the river plumes whose high-variability sections are dominated by discharge, SSS anomalies can be used to infer discharge.

5.2. Implications for future work

Accurate observation of global continental discharge is a crucial first step towards understanding and closing the global water budget. With declining gaging stations observations, new methods of acquiring discharge information are needed. The two methods we provided are completely based on satellite and remote sensing data. Though satellite data are of short-term record, they offer global coverage. Mass change and sea surface height observations are expected to continue with the planned launch of the GRACE Follow On Mission in 2017 and multiple existing and planned ocean altimetry missions. Subsurface temperature and salinity information from ARGO floats has allowed a big improvement in the estimation of thermal expansion-induced sea height change.

Currently, the biggest challenge in estimating discharge from the mass-balance is *E-P*. Evapotranspiration (evaporation) over land (ocean) is perhaps the most difficult water cycle component to quantify and this is likely to be the case in the foreseeable future. However, moisture convergences from reanalysis products provide a very reliable proxy for estimating *E-P*. The next generation reanalysis products are likely to benefit from increased observations

available from satellites, aircrafts and ground measurements. Thus, even though accuracy in GRACE is not likely to increase, since it is constrained by the orbit, and the strength of the mass anomaly signal rather than instrument error, improved estimates of *E-P* are likely to bring the mass-balance estimates closer to the 'truth'.

Similarly, satellite observation of SSS, with increased frequency and resolution, would benefit estimating discharge through correlation with SSS. While the Aquarius mission ended in 2015, SMOS and the recently launched SMAP missions would continue providing SSS retrievals. Both these methods would be useful to, and benefit from, the launch of SWOT mission, which would be able to provide highly accurate and detailed estimates of river discharge. In basins where accurate measurements of basin discharge are available, the methods can be used to estimate subsurface groundwater flux into ocean- one of the most difficult to measure components of the hydrologic cycle.

The sensitivity experiments provided in Chapter 3 have important implications on ocean-ice modeling. The inaccuracies in discharge would help explain a fraction of model-observation mismatch. The experiments highlight which regions are sensitive to changes in ocean dynamics, and which rivers suffer from higher discharge inaccuracies. The experiments with mass-balance estimates can be repeated after extending time duration (with climatological *dM/dt*) in order to understand the ocean response to these forcing at interannual scales. The experiments can be expanded to analyze fields such as barrier layer thickness, oceanic heat uptake, deep water formation, meridional overturning circulation, air-sea CO_2 flux, and oxygen minimum zones. Further detailed analysis can be performed at regional scales, such as the effect of freshening in the Arctic Ocean.

Similar sensitivity experiments can be conducted regarding the expected changes in the global discharge, under different emission scenarios. Fully coupled experiments can be conducted by simulating large-scale water management infrastructure, such as the planned country-wide river linking project by the Government of India, in order to analyze how the ocean responds, and whether changes in discharge would result in further changes in discharge due to a potential discharge feedback loop.

References

Aagaard, K., and E. C. Carmack (1989), The Role of Sea Ice and Other Fresh Water in the Arctic Circulation, *J. Geophys. Res.*, *94*(C10), 14485–14498, doi:10.1029/JC094iC10p14485.

Adler, R. F. et al. (2003), The Version-2 Global Precipitation Climatology Project (GPCP) Monthly Precipitation Analysis (1979–Present), *J. Hydrometeorol.*, *4*(6), 1147–1167, doi:10.1175/1520-0477(1997)078<0005:TGPCPG>2.0.CO;2.

Akhil, V. P., F. Durand, M. Lengaigne, J. Vialard, M. G. Keerthi, V. V. Gopalakrishna, C. Deltel, F. Papa, and C. de Boyer Montégut (2014), A modeling study of the processes of surface salinity seasonal cycle in the Bay of Bengal, *J. Geophys. Res. Ocean.*, *119*(6), 3926–3947, doi:10.1002/2013JC009632.

Alory, G., C. Maes, T. Delcroix, N. Reul, and S. Illig (2012), Seasonal dynamics of sea surface salinity off Panama: The far Eastern Pacific Fresh Pool, *J. Geophys. Res. Ocean.*, *117*(C4), n/a–n/a, doi:10.1029/2011JC007802.

Alsdorf, D. E., E. Rodríguez, and D. P. Lettenmaier (2007), Measuring surface water from space, *Rev. Geophys.*, *45*(2).

AVISO (2015), *SSALTO/DUACS User Handbook: (M)SLA and (M)ADT Near-Real Time and Delayed Time Products*.

de Baar, H. J. W. et al. (2005), Synthesis of iron fertilization experiments: From the iron age in the age of enlightenment, *J. Geophys. Res. C Ocean.*, *110*(9), 1–24, doi:10.1029/2004JC002601.

Bjornsson, H., and S. Venegas (1997), *A manual for EOF and SVD analyses of Climate Data*.

Bonjean, F., and G. S. E. Lagerloef (2002), Diagnostic Model and Analysis of the Surface Currents in the Tropical Pacific Ocean, *J. Phys. Oceanogr.*, *32*(10), 2938–2954, doi:10.1175/1520-0485(2002)032<2938:DMAAOT>2.0.CO;2.

Bosilovich, M. G., R. Lucchesi, and M. Suarez (2015), MERRA-2: File Specification. GMAO Office Note No. 9 (Version 1.0), 73 pp, available from http://gmao.gsfc.nasa.gov/pubs/office_notes, , *available*.

de Boyer Montégut, C., J. Mignot, A. Lazar, and S. Cravatte (2007), Control of salinity on the mixed layer depth in the world ocean: 1. General description, *J. Geophys. Res.*, *112*(C6), C06011, doi:10.1029/2006JC003953.

Campbell, D. (2005), The Congo River Basin, *world Larg. Wetl. Ecol.* ….

Capotondi, A., M. A. Alexander, N. A. Bond, E. N. Curchitser, and J. D. Scott (2012), Enhanced upper ocean stratification with climate change in the CMIP3 models, *J. Geophys. Res. Ocean.*, *117*(4), 1–23, doi:10.1029/2011JC007409.

Chaitanya, A. V. S., M. Lengaigne, J. Vialard, V. V. Gopalakrishna, F. Durand, C. Kranthikumar, S. Amritash, V. Suneel, F. Papa, and M. Ravichandran (2014), Salinity Measurements Collected by Fishermen Reveal a "River in the Sea" Flowing Along the Eastern Coast of India, *Bull. Am. Meteorol. Soc.*, *95*(12), 1897–1908, doi:10.1175/BAMS-D-12-00243.1.

Chambers, D. P., J. Wahr, and R. S. Nerem (2004), Preliminary observations of global ocean mass variations with GRACE, *Geophys. Res. Lett.*, *31*(13), n/a–n/a, doi:10.1029/2004GL020461.

Chao, Y., J. D. Farrara, G. Schumann, K. M. Andreadis, and D. Moller (2015), Sea surface

salinity variability in response to the Congo river discharge, *Cont. Shelf Res.*, *99*, 35–45, doi:10.1016/j.csr.2015.03.005.
Clark, E. a., J. Sheffield, M. T. H. van Vliet, B. Nijssen, and D. P. Lettenmaier (2015), Continental Runoff into the Oceans (1950–2008), *J. Hydrometeorol.*, *16*(4), 1502–1520, doi:10.1175/JHM-D-14-0183.1.
Couet, Thomas De, and T. Maurer (2009), *Surface Freshwater Fluxes into the World Oceans / Thomas de Couet; Thomas Maurer. Global Runoff Data Centre*, Federal Institute of Hydrology (BfG).
Curry, J. A. et al. (2004), Seaflux, *Bull. Am. Meteorol. Soc.*, *85*(3), 409–424.
Dai, A., and K. E. Trenberth (2002), Estimates of Freshwater Discharge from Continents: Latitudinal and Seasonal Variations, *J. Hydrometeorol.*, *3*(6), 660–687.
Dai, A., T. Qian, K. E. Trenberth, and J. D. Milliman (2009), Changes in continental freshwater discharge from 1948 to 2004, *J. Clim.*, *22*(10), 2773–2792, doi:10.1175/2008JCLI2592.1.
Danabasoglu, G., S. C. Bates, B. P. Briegleb, S. R. Jayne, M. Jochum, W. G. Large, S. Peacock, and S. G. Yeager (2012), The CCSM4 ocean component, *J. Clim.*, *25*(5), 1361–1389, doi:10.1175/JCLI-D-11-00091.1.
Danabasoglu, G. et al. (2014), North Atlantic simulations in Coordinated Ocean-ice Reference Experiments phase II (CORE-II). Part I: Mean states, *Ocean Model.*, *73*, 76–107.
Danabasoglu, G. et al. (2016), North Atlantic simulations in Coordinated Ocean-ice Reference Experiments phase II (CORE-II). Part II: Inter-annual to decadal variability, *Ocean Model.*, *97*, 65–90, doi:10.1016/j.ocemod.2015.11.007.
Davis, R. E., J. T. Sherman, and J. Dufour (2001), Profiling ALACEs and Other Advances in Autonomous Subsurface Floats, *J. Atmos. Ocean. Technol.*, *18*(6), 982–993, doi:10.1175/1520-0426(2001)018<0982:PAAOAI>2.0.CO;2.
Dee, D. P. et al. (2011), The ERA-Interim reanalysis: Configuration and performance of the data assimilation system, *Q. J. R. Meteorol. Soc.*, *137*(656), 553–597, doi:10.1002/qj.828.
Dong, S., S. L. Garzoli, and M. Baringer (2009), An assessment of the seasonal mixed layer salinity budget in the Southern Ocean, *J. Geophys. Res. Ocean.*, *114*(12), doi:10.1029/2008JC005258.
Durand, M., L.-L. Fu, D. P. Lettenmaier, D. E. Alsdorf, E. Rodriguez, and D. Esteban-Fernandez (2010), The Surface Water and Ocean Topography Mission: Observing Terrestrial Surface Water and Oceanic Submesoscale Eddies, *Proc. IEEE*, *98*(5), 766–779, doi:10.1109/JPROC.2010.2043031.
Famiglietti, J. S., and E. F. Wood (1994), Multiscale modeling of spatially variable water and energy balance processes, *Water Resour. Res.*, *30*(11), 3061–3078, doi:10.1029/94WR01498.
Fekete, B. M. (2002), High-resolution fields of global runoff combining observed river discharge and simulated water balances, *Global Biogeochem. Cycles*, *16*(3), 15-1-15-10
Foltz, G. R., and M. J. McPhaden (2008), Seasonal mixed layer salinity balance of the tropical North Atlantic Ocean, *J. Geophys. Res.*, *113*(C2), C02013, doi:10.1029/2007JC004178.
Fong, D. A., and W. R. Geyer (2001), Response of a river plume during an upwelling favorable wind event, *J. Geophys. Res.*, *106*(C1), 1067, doi:10.1029/2000JC900134.
Fournier, S., T. Lee, and M. M. Gierach (2016), Seasonal and interannual variations of sea surface salinity associated with the Mississippi River plume observed by SMOS and Aquarius, *Remote Sens. Environ.*, *180*, 431–439, doi:10.1016/j.rse.2016.02.050.
Gao, S., T. Qu, and X. Nie (2014), Mixed layer salinity budget in the tropical Pacific Ocean

estimated by a global GCM, *J. Geophys. Res. Ocean.*, *119*(12), 8255–8270, doi:10.1002/2014JC010336.
Gent, P. R. et al. (2011), The community climate system model version 4, *J. Clim.*, *24*(19), 4973–4991, doi:10.1175/2011JCLI4083.1.
Gierach, M. M., J. Vazquez-Cuervo, T. Lee, and V. M. Tsontos (2013), Aquarius and SMOS detect effects of an extreme Mississippi River flooding event in the Gulf of Mexico, *Geophys. Res. Lett.*, *40*(19), 5188–5193, doi:10.1002/grl.50995.
Gleason, C. J., and L. C. Smith (2014), Toward global mapping of river discharge using satellite images and at-many-stations hydraulic geometry., *Proc. Natl. Acad. Sci. U. S. A.*, 1317606111–, doi:10.1073/pnas.1317606111.
Good, S. A., M. J. Martin, and N. A. Rayner (2013), EN4: Quality controlled ocean temperature and salinity profiles and monthly objective analyses with uncertainty estimates, *J. Geophys. Res. Ocean.*, *118*(12), 6704–6716, doi:10.1002/2013JC009067.
GRDC (2015), Temporal Distribution of Global River Discharge Data
Griffies, S. M., M. Winton, B. Samuels, G. Danabasoglu, S. Yeager, S. Marlsand, H. Drange., and M. Bentsen (2012), Project Report Datasets and protocol for the CLIVAR WGOMD Coordinated Ocean-sea ice Reference Experiments (COREs) October 2012, *WCRP Rep. No. 21/2012*, (184), 21.
Griffies, S. M. et al. (2014), An assessment of global and regional sea level for years 1993–2007 in a suite of interannual CORE-II simulations, *Ocean Model.*, *78*, 35–89, doi:10.1016/j.ocemod.2014.03.004.
Grodsky, S. A., G. Reverdin, J. A. Carton, and V. J. Coles (2014), Year-to-year salinity changes in the Amazon plume: Contrasting 2011 and 2012 Aquarius/SACD and SMOS satellite data, *Remote Sens. Environ.*, *140*, 14–22, doi:10.1016/j.rse.2013.08.033.
Hasson, A. E. a, T. Delcroix, and R. Dussin (2013), An assessment of the mixed layer salinity budget in the tropical Pacific Ocean. Observations and modelling (1990-2009), *Ocean Dyn.*, *63*(2-3), 179–194, doi:10.1007/s10236-013-0596-2.
Hellweger, F. L., and A. L. Gordon (2002), Tracing Amazon River water into the Caribbean Sea, *J. Mar. Res.*, *60*(4), 537–549, doi:10.1357/002224002762324202.
Holland, M. M., D. A. Bailey, B. P. Briegleb, B. Light, and E. Hunke (2012), Improved Sea Ice Shortwave Radiation Physics in CCSM4: The Impact of Melt Ponds and Aerosols on Arctic Sea Ice*, *J. Clim.*, *25*(5), 1413–1430, doi:10.1175/JCLI-D-11-00078.1.
Hopkins, J., M. Lucas, C. Dufau, M. Sutton, J. Stum, O. Lauret, and C. Channelliere (2013), Detection and variability of the Congo River plume from satellite derived sea surface temperature, salinity, ocean colour and sea level, *Remote Sens. Environ.*, *139*, 365–385, doi:10.1016/j.rse.2013.08.015.
Hurrell, J. W. et al. (2013), The community earth system model: A framework for collaborative research, *Bull. Am. Meteorol. Soc.*, *94*(9), 1339–1360, doi:10.1175/BAMS-D-12-00121.1.
Ibánhez, J. S. P., M. Araujo, and N. Lefèvre (2016), The overlooked tropical oceanic CO 2 sink, *Geophys. Res. Lett.*, 43(8), 3804-3812, doi:10.1002/2016GL068020.
IOC, SCOR, and IAPSO (2010), *The international thermodynamic equation of seawater-2010: Calculation and use of thermodynamic properties*, UNESCO.
Kay, J. E. et al. (2015), The Community Earth System Model (CESM) Large Ensemble Project: A Community Resource for Studying Climate Change in the Presence of Internal Climate Variability, *Bull. Am. Meteorol. Soc.*, *96*(8), 1333–1349, doi:10.1175/BAMS-D-13-00255.1.
Kobayashi, S. et al. (2015), The JRA-55 Reanalysis: General Specifications and Basic

Characteristics, *J. Meteorol. Soc. Japan. Ser. II*, *93*(1), 5–48, doi:10.2151/jmsj.2015-001.
Körtzinger, A. (2003), A significant CO2 sink in the tropical Atlantic Ocean associated with the Amazon River plume, *Geophys. Res. Lett.*,30, 2287.
Labat, D., J. Ronchail, and J. L. Guyot (2005), Recent advances in wavelet analyses: Part 2—Amazon, Parana, Orinoco and Congo discharges time scale variability, *J. Hydrol.*, *314*(1-4), 289–311, doi:10.1016/j.jhydrol.2005.04.004.
Large, W. G., and S. G. Yeager (2009), The global climatology of an interannually varying air - Sea flux data set, *Clim. Dyn.*, *33*(2-3), 341–364, doi:10.1007/s00382-008-0441-3.
Lawrence, D. M., A. G. Slater, and S. C. Swenson (2012), Simulation of Present-Day and Future Permafrost and Seasonally Frozen Ground Conditions in CCSM4, *J. Clim.*, *25*(7), 2207–2225, doi:10.1175/JCLI-D-11-00334.1.
Lee, H., R. E. Beighley, D. Alsdorf, H. C. Jung, C. K. Shum, J. Duan, J. Guo, D. Yamazaki, and K. Andreadis (2011), Characterization of terrestrial water dynamics in the Congo Basin using GRACE and satellite radar altimetry, *Remote Sens. Environ.*, *115*(12), 3530–3538, doi:10.1016/j.rse.2011.08.015.
Levitus, S., J. I. Antonov, T. P. Boyer, R. a. Locarnini, H. E. Garcia, and a. V. Mishonov (2009), Global ocean heat content 1955-2008 in light of recently revealed instrumentation problems, *Geophys. Res. Lett.*, *36*(7), n/a–n/a, doi:10.1029/2008GL037155.
Meeuwis, J. M., J. R. E. Lutjeharms, and A. R. E. Lutjeharmst (1990), Surface thermal characteristics of the Angola- Benguela front, *South African J. Mar. Sci.*, *9*(1), 261–279, doi:10.2989/025776190784378772.
Mersel, M. K., L. C. Smith, K. M. Andreadis, and M. T. Durand (2013), Estimation of river depth from remotely sensed hydraulic relationships, *Water Resour. Res.*, *49*(6), 3165–3179, doi:10.1002/wrcr.20176.
Mignot, J., C. de Boyer Montégut, A. Lazar, and S. Cravatte (2007), Control of salinity on the mixed layer depth in the world ocean: 2. Tropical areas, *J. Geophys. Res.*, *112*(C10), C10010, doi:10.1029/2006JC003954.
Milly, P. C. D., K. A. Dunne, and A. V. Vecchia (2005), Global pattern of trends in streamflow and water availability in a changing climate., *Nature*, *438*(7066), 347–350, doi:10.1038/nature04312.
Moore, J. K., S. C. Doney, and K. Lindsay (2004), Upper ocean ecosystem dynamics and iron cycling in a global three-dimensional model, *Global Biogeochem. Cycles*, *18*(4), n/a–n/a, doi:10.1029/2004GB002220.
North, G. R., T. L. Bell, R. F. Cahalan, and F. J. Moeng (1982), Sampling Errors in the Estimation of Empirical Orthogonal Functions, *Mon. Weather Rev.*, *110*(7), 699–706, doi:10.1175/1520-0493(1982)110<0699:SEITEO>2.0.CO;2.
Oki, T., and S. Kanae (2006), Global hydrological cycles and world water resources., *Science*, *313*(5790), 1068–1072, doi:10.1126/science.1128845.
Oleson, K. W. et al. (2004), Technical Description of the Community Land Model (CLM), *NCAR Tech. Note*, *NCAR/TN-46*(April), 186, doi:10.5065/D6N877R0.
Rao, R. R., and R. Sivakumar (2003), Seasonal variability of sea surface salinity and salt budget of the mixed layer of the north Indian Ocean, *J. Geophys. Res.*, *108*(C1), 3009, doi:10.1029/2001JC000907.
Reul, N. et al. (2014), Sea Surface Salinity Observations from Space with the SMOS Satellite: A New Means to Monitor the Marine Branch of the Water Cycle, *Surv. Geophys.*, *35*(3), 681–722, doi:10.1007/s10712-013-9244-0.

Rienecker, M. M. et al. (2011), MERRA: NASA's modern-era retrospective analysis for research and applications, *J. Clim.*, *24*(14), 3624–3648, doi:10.1175/JCLI-D-11-00015.1.
Rignot, E., I. Velicogna, M. R. Van Den Broeke, a. Monaghan, and J. Lenaerts (2011a), Acceleration of the contribution of the Greenland and Antarctic ice sheets to sea level rise, *Geophys. Res. Lett.*, *38*(5), 1–5, doi:10.1029/2011GL046583.
Rignot, E., I. Velicogna, M. R. van den Broeke, A. Monaghan, and J. T. M. Lenaerts (2011b), Acceleration of the contribution of the Greenland and Antarctic ice sheets to sea level rise., *Geophys. Res. Lett.*, *38*(5), 417–23, doi:10.1029/2011GL046583.
Rignot, E. et al. (2011c), Ice flow of the Antarctic ice sheet., *Science*, *333*(6048), 1427–30, doi:10.1126/science.1208336.
Rodell, M. et al. (2015), The Observed State of the Water Cycle in the Early 21st Century, *J. Clim.*, 8289–8318, doi:10.1175/JCLI-D-14-00555.1.
Saha, S. et al. (2010), The NCEP Climate Forecast System Reanalysis, *Bull. Am. Meteorol. Soc.*, *91*(8), 1015–1057, doi:10.1175/2010BAMS3001.1.
Sprintall, J., and M. Tomczak (1992), Evidence of the barrier layer in the surface layer of the tropics, *J. Geophys. Res.*, *97*(C5), 7305.
Subramaniam, A. et al. (2008), Amazon River enhances diazotrophy and carbon sequestration in the tropical North Atlantic Ocean, *Proc. Natl. Acad. Sci.*, *105*(30), 10460–10465, doi:10.1073/pnas.0710279105.
Syed, T. H., J. S. Famiglietti, J. Chen, M. Rodell, S. I. Seneviratne, P. Viterbo, and C. R. Wilson (2005a), Total basin discharge for the Amazon and Mississippi River basins from GRACE and a land-atmosphere water balance, *Geophys. Res. Lett.*, *32*(24), L24404, doi:10.1029/2005GL024851.
Syed, T. H., J. S. Famiglietti, J. Chen, M. Rodell, S. I. Seneviratne, P. Viterbo, and C. R. Wilson (2005b), Total basin discharge for the Amazon and Mississippi River basins from GRACE and a land-atmosphere water balance, *Geophys. Res. Lett.*, *32*(24), 1–5, doi:10.1029/2005GL024851.
Syed, T. H., J. S. Famiglietti, and D. P. Chambers (2009), GRACE-Based Estimates of Terrestrial Freshwater Discharge from Basin to Continental Scales, *J. Hydrometeorol.*, *10*(1), 22–40, doi:10.1175/2008JHM993.1.
Syed, T. H., J. S. Famiglietti, D. P. Chambers, J. K. Willis, and K. Hilburn (2010), Satellite-based global-ocean mass balance estimates of interannual variability and emerging trends in continental freshwater discharge., *Proc. Natl. Acad. Sci. U. S. A.*, *107*(42), 17916–17921, doi:10.1073/pnas.1003292107.
Trenberth, K. E., and J. T. Fasullo (2013a), North American water and energy cycles, *Geophys. Res. Lett.*, *40*(2), 365–369, doi:10.1002/grl.50107.
Trenberth, K. E., and J. T. Fasullo (2013b), Regional Energy and Water Cycles: Transports from Ocean to Land, *J. Clim.*, *26*(20), 7837–7851, doi:10.1175/JCLI-D-13-00008.1.
Trenberth, K. E., L. Smith, T. Qian, A. Dai, and J. Fasullo (2007), Estimates of the Global Water Budget and Its Annual Cycle Using Observational and Model Data, *J. Hydrometeorol.*, *8*(4), 758–769, doi:10.1175/JHM600.1.
Trenberth, K. E., J. T. Fasullo, and J. Mackaro (2011), Atmospheric moisture transports from ocean to land and global energy flows in reanalyses, *J. Clim.*, *24*(18), 4907–4924, doi:10.1175/2011JCLI4171.1.
Le Vine, D. M., G. S. E. Lagerloef, F. R. Colomb, S. H. Yueh, and F. a. Pellerano (2007), Aquarius: An instrument to monitor sea surface salinity from space, *IEEE Trans. Geosci.*

Remote Sens., *45*(7), 2040–2050, doi:10.1109/TGRS.2007.898092.

Le Vine, D. M., P. de Matthaeis, C. S. Ruf, and D. D. Chen (2014), Aquarius RFI detection and mitigation algorithm: Assessment and examples, *Geosci. Remote Sensing, IEEE Trans.*, *52*(8), 4574–4584.

Wang, K., and R. E. Dickinson (2012), A review of global terrestrial evapotranspiration: Observation, modeling, climatology, and climatic variability, *Rev. Geophys.*, *50*(2), RG2005, doi:10.1029/2011RG000373.

Watkins, M. M., D. N. Wiese, D.-N. Yuan, C. Boening, and F. W. Landerer (2015), Improved methods for observing Earth's time variable mass distribution with GRACE using spherical cap mascons, *J. Geophys. Res. Solid Earth*, *120*(4), 2648–2671, doi:10.1002/2014JB011547.

Xie, P., and P. A. Arkin (1997), Global Precipitation: A 17-Year Monthly Analysis Based on Gauge Observations, Satellite Estimates, and Numerical Model Outputs, *Bull. Am. Meteorol. Soc.*, *78*(11), 2539–2558, doi:http://dx.doi.org/10.1175/1520-0477(1997)078<2539:GPAYMA>2.0.CO;2.

Yamazaki, D., S. Kanae, H. Kim, and T. Oki (2011), A physically based description of floodplain inundation dynamics in a global river routing model, *Water Resour. Res.*, *47*(4), n/a–n/a, doi:10.1029/2010WR009726.

Yu, L. (2014), Coherent evidence from Aquarius and Argo for the existence of a shallow low-salinity convergence zone beneath the Pacific ITCZ, *J. Geophys. Res. Ocean.*, *119*(11), 7625–7644.

Yu, L., X. Jin, and R. A. Weller (2008), *Multidecade Global Flux Datasets from the Objectively Analyzed Air-sea Fluxes (OAFlux) Project: Latent and Sensible Heat Fluxes, Ocean Evaporation, and Related Surface Meteorological Variables*.

Yueh, S., W. Tang, A. Fore, A. Hayashi, Y. T. Song, and G. Lagerloef (2014), Aquarius geophysical model function and combined active passive algorithm for ocean surface salinity and wind retrieval, *J. Geophys. Res. Ocean.*, *119*(8), 5360–5379, doi:10.1002/2014JC009939.

Zaitchik, B. F., M. Rodell, and F. Olivera (2010), Evaluation of the Global Land Data Assimilation System using global river discharge data and a source-to-sink routing scheme, *Water Resour. Res.*, *46*(6), W06507, doi:10.1029/2009WR007811.

Appendix

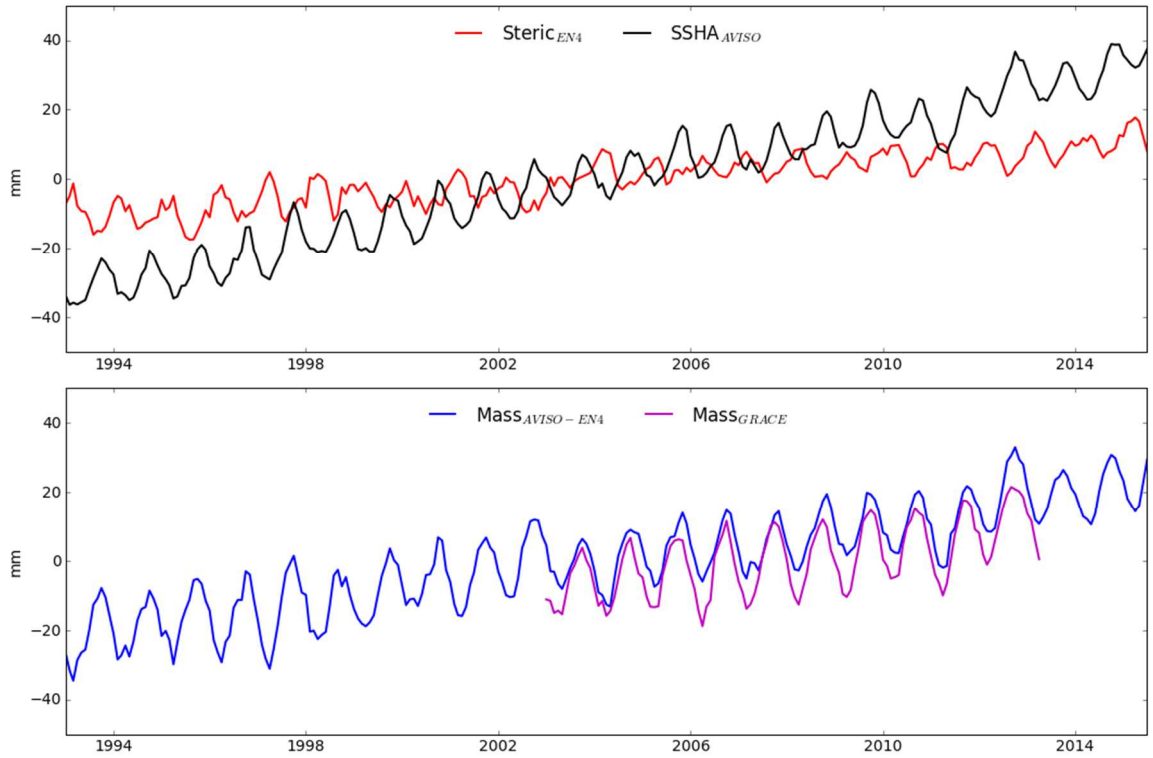


Figure A1. (top) Monthly time series of Sea Surface Height Anomaly (SSHA, black) from AVISO Ssalto/Duacs merged mulit-mission altimetry data, and Steric Height Anomaly (SHA, red) from Hadley Center EN4 subsurface temperature and salinity fields. (bottom) Time series of ocean mass derived from SSHA and SHA (blue), and from GRACE (magenta)

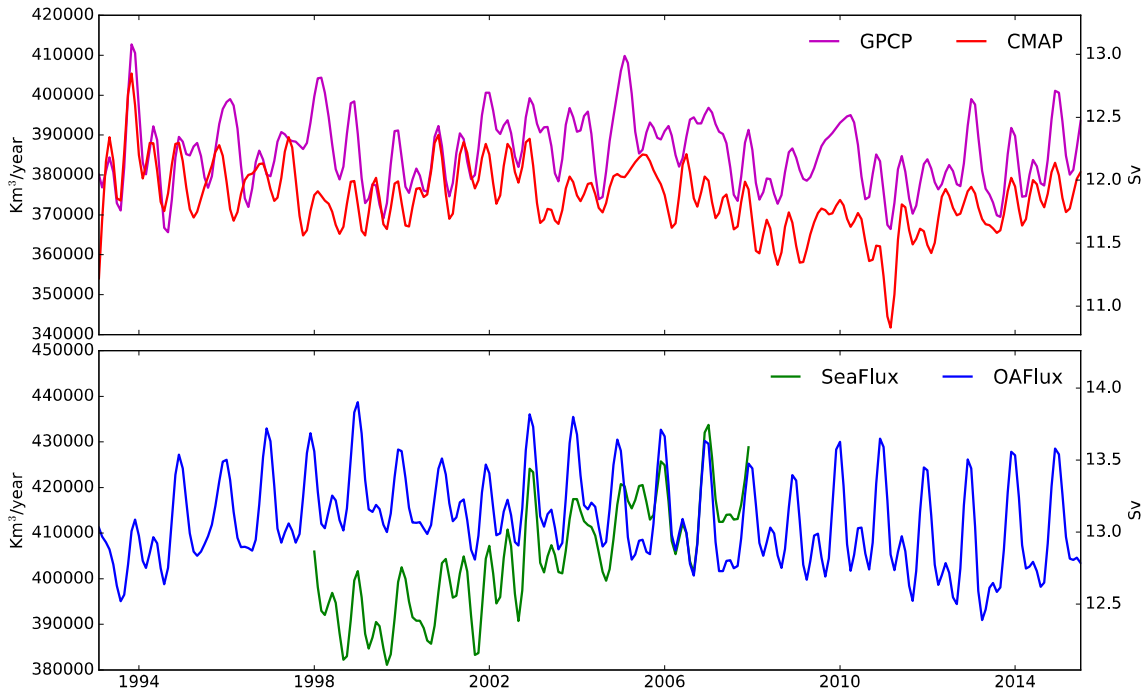


Figure A2. The time series of remote sensing-based data of global ocean precipitation (top), and evaporation (bottom)